Boone Samuel, C (Orcid ID: 0000-0003-2274-7933)
Balestrieri Maria-Laura (Orcid ID: 0000-0002-8652-0845)
Kohn Barry, P. (Orcid ID: 0000-0001-5064-5454)
Corti Giacomo (Orcid ID: 0000-0001-7399-4438)
Gleadow Andrew, J.W. (Orcid ID: 0000-0003-0496-0028)

Tectono-thermal evolution of the Broadly Rifted Zone, Ethiopian Rift

S. C. Boone[1, 2], M. -L. Balestrieri[3], B. P. Kohn[1], G. Corti[3], A. J. W. Gleadow[1], and C. Seiler[4]

[1]School of Earth Sciences, University of Melbourne, VIC 3010, Australia
[2]Now at Institute of Geosciences, Johannes Gutenberg University Mainz, 55099 Mainz, Germany
[3]Istituto di Geoscienze e Georisorse, Consiglio Nazionale delle Ricerche, UOS Firenze, via G. La Pira 4, 50121, Firenze, Italia
[4]Geoscience Australia, GPO Box 378, Canberra, ACT 2601, Australia

Corresponding author: Samuel C. Boone (samcboone@gmail.com)

Key Points:

- Apatite (U-Th-Sm)/He and augmented fission track data constrain early Miocene onset of rift-related cooling in Beto and Galana basin margins
- Contrasting along-strike cooling histories of Beto and Galana margins appear to reflect disparate structural geometries of their basin-bounding fault arrays
- Longitudinal contrasts in structural evolution of Broadly Rifted Zone may result from E-W differences in pre-existing lithospheric heterogeneities

Abstract

The Broadly Rifted Zone (BRZ) of southern Ethiopia is a long-lived and structurally complex segment of the East African Rift System (EARS). However, due to poor surface exposure of early syn-rift strata and a dearth of subsurface data, the evolution of the BRZ remains poorly understood. We present new apatite (U-Th-Sm)/He and augmented apatite fission track low-temperature thermochronology data from the Beto and Galana basin boundary fault systems to constrain the tectono-thermal evolution of the western and eastern BRZ, respectively. Time-temperature reconstructions suggest that EARS-related extension began concurrently across the BRZ in the early Miocene (20-17 Ma), at least 6 Myr prior to faulting in the Main Ethiopian Rift further north. Increased time-temperature resolution provided by multi-thermochronometer analyses reveals contrasting along-strike spatiotemporal variations in Beto and Galana margin cooling histories, which appear to mirror the disparate structural geometries of their basin-bounding normal fault arrays. Longitudinal contrasts in basin architecture and rift-related cooling histories across the BRZ may reflect the region's heterogeneous distribution of pre-existing basement fabrics, namely the presence of a

This is the author manuscript accepted for publication and has undergone full peer review but has not been through the copyediting, typesetting, pagination and proofreading process, which may lead to differences between this version and the Version of Record. Please cite this article as doi: 10.1029/2018TC005210

previously reported N-NNE trending Neoproterozoic suture zone beneath the eastern BRZ. Its influence may explain both the development of long, curvilinear faults and the gradual basin-wards migration of strain exhibited by the easternmost BRZ, absent further west. The anomalous evolution of the BRZ compared to the greater Ethiopian Rift, both in its earlier onset and its wider deformation zone, likely results from its inheritance of pre-attenuated lithosphere, thermo-mechanically modified by earlier Cretaceous-Paleogene Anza-South Sudan rifting and/or Eocene plume impingement.

1 Introduction

Investigations into the evolution of boundary fault systems in extensional tectonic settings can provide valuable information regarding paleo-plate boundary conditions and the rheological structure of the deformed lithosphere during rift evolution. Field studies and numerical and analogue models have shown that the way in which normal fault systems grow reflects the mechanical, thermal and kinematic properties of the deforming lithosphere, and rift boundary conditions [e.g. *Bürgmann et al.*, 1994; *Steen and Andresen*, 1999; *Wilkins and Gross*, 2002; *Childs et al.*, 2009; *Jackson and Rotevatn*, 2013]. If formed in association with magmatism, fault nucleation and growth may also reflect local changes in rheology and stress regime caused by magma emplacement and related volatile release [e.g. *Ebinger and Casey*, 2001; *Corti et al*., 2003; *Tentler*, 2005; *Rowland et al*., 2007; *Muirhead et al*., 2016]. Moreover, the migration of activity along and between basin bounding fault systems provides insight into rift-scale evolutionary trends and strain localisation processes [*Gawthorpe et al.*, 2003]. Yet, determining the temporal evolution of a fault system from structural analysis of its final configuration alone is difficult due to displacement profile readjustment processes, which conceal the relative timing of strain accommodation [*Commins et al.*, 2005]. Alternative methods are, thus, often used to help constrain spatio-temporal displacement accumulation trends, such as sequence stratigraphy [e.g. *Gawthorpe et al.*, 1997; *Davies et al.*, 2000; *Dawers and Underhill*, 2000] and seismic techniques [e.g. *Morley*, 1999a; *Morley and Wescott*, 1999; *Mcleod et al.*, 2000]. However, in instances where little control on syn-rift stratigraphy and sub-surface basin architecture exist, the predictable pattern of footwall uplift and denudation in response to lateral fault growth and displacement accumulation can instead be used to elucidate normal fault array evolution [*Harbor*, 1997; *Densmore et al.*, 2004, 2007].

Such is the case for the Broadly Rifted Zone (BRZ) of southern Ethiopia (Figure 1), a long-lived and structurally complex part of the greater East African Rift System (EARS). While the EARS is primarily comprised of a narrow (~100 km) corridor of middle-late Miocene aged grabens and half-grabens, active deformation in the BRZ is diffused over a much broader region (as wide as ~300km) in a series of basins and ranges that extends into the Turkana Depression of northern Kenya [*Baker et al.*, 1972; *Davidson and Rex*, 1980]. Moreover, field mapping, structural geology and thermochronological studies suggest that EARS extensional deformation began earlier in the Turkana Depression (late Paleogene) and BRZ (early Miocene) than in the Main Ethiopian Rift (MER) and Kenyan Rift to the north and south [*Balestrieri et al.*, 2016; *Boone et al.*, 2018b; *Woldegabriel and Aronson*, 1987; *Morley et al.*, 1992, 1999b, *Ebinger et al.*, 1993, 2000; *Pik et al.*, 2008]. Unlike the MER and Kenyan Rift, where volcano-tectonic activity is well documented, the evolution of the BRZ is, by comparison, poorly constrained due to a relative scarcity of geological observations and subsurface data.

Low-temperature thermochronometers, such as apatite fission track (AFT) analysis, are alternative, yet powerful, tools to constrain periods of rift basin development by determining the timing of denudation and cooling associated with rift-related footwall uplift [e.g.

Fitzgerald, 1992; *Stockli*, 2005; *Storti et al.*, 2008]. While the well-understood behaviour of the AFT system makes it a robust method for constraining the timing and degree of cooling related to extensional tectonism [*Kohn et al.*, 2005], in certain cases its temperature sensitivity (~60-120 °C) can be too high to adequately record small-amplitude variations in footwall cooling histories associated with normal fault slip [*Brown et al.*, 2017]. Such was the case for previous thermochronology studies in the BRZ [*Philippon et al*., 2014; *Balestrieri et al.*, 2016], where AFT data provided minimum age constraints for the formation of the Beto Basin (between 14-10 Ma) and the Galana Basin (~10-8 Ma), bound by the Amaro Horst along its western margin. However, the onset of rift-related cooling for many samples, such as those from the southern Amaro Horst, was poorly constrained due to Neogene exhumation rates being insufficient to be recorded by the temperature sensitivity of the AFT system. The lower temperature sensitivity apatite (U-Th-Sm)/He (AHe) system (~30-90 °C) provides an alternative thermochronometer, better suited to be able to record low-magnitude tectono-thermal processes in the upper ~1-2 km of the crust that might otherwise be poorly resolved by AFT analyses alone [*Stockli et al.*, 2000; *Balestrieri et al.*, 2005].

Here, we present combined AFT and AHe analyses and thermal history modelling results from the Beto and Galana Basins (Amaro Horst region) from the western and eastern BRZ, respectively. These data reveal along-strike footwall cooling history trends for the fault systems bounding these basins, providing new constraints for the onset of extensional deformation and propagation of strain in the BRZ. The mechanical, thermal and kinematic parameters that controlled the structural evolution of the BRZ are also explored.

2 Geological Setting

The late Paleogene-Recent EARS is widely considered to be the archetypal magma-assisted continental rift, having developed diachronously above an elongate mantle plume impinged beneath East Africa in the Eocene [e.g. *Ebinger and Sleep*, 1998; *Bastow et al.*, 2005, 2011; *Benoit et al.*, 2006; *Fishwick*, 2010]. Subsequent extensional deformation preferentially followed a trend of Late Archean-Proterozoic mobile belts, circumventing stronger cratonic regions [*Mohr*, 1962; *McConnell*, 1972; *Daly et al.*, 1989; *Smith and Mosley*, 1993; *Hetzel and Strecker*, 1994].

The Ethiopian Rift represents a key sector of the EARS, defining the incipient boundary between the Nubian and Somalian plates [*Chorowicz*, 2005]. Along its ~1000 km length, it encompasses multiple rift segments at varying stages of continental breakup, exhibiting a general southwards decrease in rift maturity [*Ebinger*, 2005]. Rift localization and evolution are thought to have been strongly controlled by the presence of a N-NNE trending suture zone within the Neoproterozoic Mozambique Belt [*Bastow et al.*, 2008; *Keranen and Klemperer*, 2008; *Keranen et al.*, 2009], interpreted to mark an important crustal boundary between juvenile crust to the west from reworked Paleoproterozoic-Archean crust to the east [*Berhe*, 1990; *Stern et al.*, 1990; *Stern*, 2002].

Analyses of the modern day stress field suggest a current ~E-W (~N100°E) extension direction between the Nubian and Somalian plates [*Bosworth et al.*, 1992; *Foster and Jackson*, 1998; *Fernandes et al.*, 2004; *Bendick et al.*, 2006; *Keir et al.*, 2006; *Saria et al.*, 2014]. Although, it is disputed whether these kinematic boundary conditions have remained constant during the entirety of rift evolution [*Corti*, 2009 and references therein], with some authors arguing for a poly-phase history involving a change in plate motion direction at some time during the interval 6.6-2.6 Ma [*Bonini et al.*, 1997, 2005; *Boccaletti et al.*, 1998]. More recent studies however, suggest that the ~E-W extension direction in the Ethiopian Rift has likely remained constant since at least 11 Ma, with estimates of earlier plate kinematics being limited by sparse coverage of magmatic reversals [*Royer et al.*, 2006; *DeMets and Merkouriev*, 2016].

2.1 Broadly Rifted Zone (BRZ)

The BRZ marks the transition from the narrow (~100 km) rift valley morphology of the MER to a diffuse zone of deformation encompassing a ~300 km wide region of basins and ranges, south of Lake Abaya (Figure 1) [*Baker et al.*, 1972; *Moore and Davidson*, 1978; *Ebinger et al.*, 2000]. This increase in physiographic complexity coincides with a southward, ~15km shallowing of the Moho attributed to Cretaceous-early Paleogene crustal attenuation beneath the NW-SE trending Anza Rift (Figure 1) [*Benoit et al.*, 2006; *Keranen and Klemperer*, 2008; *Keranen et al*., 2009; *Philippon et al*., 2014; *Brune et al*., 2017]. The region also marks the transition from the high elevations of the Ethiopian Dome (averaging 1500 m asl) to the topographically subdued Turkana Depression of northern Kenya (averaging ~600 m asl).

Between ~45-35 Ma, voluminous [30,000 km^3; *Rooney*, 2017] Eocene flood basalts erupted over much of the BRZ, representing the earliest manifestation of EARS-related volcanism in East Africa [*Morley*, 1994; *Ebinger and Sleep*, 1998]. This was followed by a Neogene-Recent period of relative volcanic quiescence in the region [*WoldeGabriel et al*., 1991; *Ebinger et al*., 1993; Corti, 2009; *Rooney*, 2017]. The onset of rift basin formation in the BRZ, however, is thought to not have occurred until much later, sometime during the Miocene [*Woldegabriel et al.*, 1991; *Ebinger et al.*, 1993, 2000; *Bonini et al.*, 2005; *Pik et al*., 2008; *Philippon et al.*, 2014; *Balestrieri et al.*, 2016].

The present-day BRZ exhibits marked longitudinal differences in structural architecture. To the west, the BRZ is comprised of a series of ~NE-SW trending blocks of Precambrian basement and Tertiary volcanic rocks tilting to the northwest, known as the Gofa Basin and Range, or Gofa Province [*Moore and Davidson*, 1978]. These are bound by highly segmented, SE-dipping normal faults [*Davidson*, 1983; *Philippon et al.*, 2014]. While further east in the Amaro Horst region, the BRZ is made up of more ~N-S trending basins delimitated by large step faults [*Ebinger et al.*, 1993]. In general, the subsurface rift architecture of the Gofa and Amaro Horst regions are poorly constrained due to a scarcity of detailed geophysical data.

2.1.1 Beto Basin

The Gofa Province is comprised of a series of ~NE-SW trending, northwest-dipping half-grabens that host alluvial and lacustrine sediments. In general, these basins widen towards the south, resulting in slightly triangular shapes in map view [*Ebinger et al.*, 2000].

One of the more prominent half-grabens in the Gofa Province is the Beto Basin (Figure 2). Its north-western margin is bound by a ~N45°E striking master fault array that extends more than 40km. The system is highly segmented and comprises a series of longer fault segments alternating with shorter, ~N150°E striking faults, giving it a distinct 'zig-zag' pattern in map view (Figure 2) [*Philippon et al*., 2014] that is typical of fault arrays that developed from the linkage of initially isolated fault segments [*Soliva and Benedicto*, 2004]. Collectively, the fault array dips steeply towards the southeast, has a maximum throw of more than 3 km [*Davidson*, 1983] and exhibits clear dip-slip kinematic indicators along its fault plane [*Philippon et al.*, 2014]. Paleostress inversion of data from the basin-bounding master fault indicates an average extensional direction of N135°E [*Philippon et al.*, 2014]. To the southwest, the Beto Basin is bound by an ~N150°E oblique-slip fault [*Ebinger et al*., 2000]. Together, the bounding fault system appears to reflect local foliation trends in the basement gneisses [~N65°E and ~N155°E; *Moore and Davidson*, 1978; Philippon *et al.*, 2014].

Faulting in the Beto Basin has exposed Precambrian basement (gneisses, amphibolites, and granulites) believed to have been deformed during the Neoproterozoic Pan-African Orogeny [*Levitte et al.*, 1974; *Davidson*, 1983; *Yemane and Yohunie*, 1987]. Basement rocks are unconformably overlain by the 45-35 Ma Amaro-Gamo basalts and Amaro tuffs [*Ebinger et al.*, 1993], which reach a collective thickness of > 1100 m in the northwest shoulder of the basin. In the footwall of the basin bounding fault, this trap series dips ~20-40° westward [*Philippon et al.*, 2014].

2.1.2 Amaro Horst region

At ~6° N, as the southern MER transitions into the eastern BRZ, the rift valley bifurcates south of Lake Abaya into two near-parallel grabens, the western Chamo (or Ganjuli) Basin and eastern Galana Basin (Figure 1). These basins are separated by the ~N-S trending Amaro Horst, a narrow (~20 km), asymmetric fault-bounded block of Precambrian basement reaching 3200 m along its eastern, steeper margin [Levitte, et al., 1974; Philippon et al., 2014].

The ~40 km wide Chamo Basin is bound to the west by a series of large step faults, whose orientations vary between ~NW-SE and ~NE-SE (Figures 1c & 2). Along its eastern margin, the Chamo Basin is bound by widely spaced, westward-dipping normal faults with small throws, which delimit the western Amaro Horst [*Ebinger et al.*, 1993; *Philippon et al*., 2014]. Basin infill is estimated to reach a total thickness of less than 2 km [*Ebinger et al.*, 1993].

By contrast, the ~30 km wide Galana Basin has an overall asymmetric, half-graben geometry, bound along its western margin by a series of ~N0°-25°E trending, steeply east-dipping step

faults that demarcate the eastern Amaro Horst (Figure 3) [*Philippon et al.*, 2014]. Here, the basin fill may reach a maximum thickness of more than 4 km [*Ebinger et al.*, 1993]. In contrast to the structural architecture of BRZ half-grabens further west, individual segments of the significantly longer (~90 km), curvilinear Galana basin-bounding fault array appear markedly more contiguous along-strike. To the east, the Galana Basin is defined by a series of W-dipping, ~N-S trending normal faults with small throws and WNW-dipping monoclines [*Ebinger et al.*, 1993]. Paleostress inversion of structural data from this region are consistent with a N94°E extension direction [*Philippon et al.*, 2014].

In the Amaro Horst region, Precambrian basement rocks, which exhibit predominantly N-S trending metamorphic foliations [*Ebinger et al.*, 1993], are unconformably overlain by discontinuous, thin (<1 m) patches of laterized gritstone and conglomerate [*Levitte et al.*, 1974]. The few outcrops of these highly eroded sedimentary rocks are too small to be shown in Figure 2. The age of these red beds is unknown, however a late Mesozoic age has been suggested by *Levitte et al*. [1974] by correlation with well-dated laterites from central Ethiopia [*Mohr*, 1962] and lithologically similar deposits from northern Turkana [*Arambourg and Wolff*, 1969]. Where present, the Amaro-Gamo basalts and Amaro tuffs (45-35 Ma) unconformably overlie Precambrian basement and the red bed regolith [*Ebinger et al.*, 1993]. These, in turn, are unconformably overlain by the 18-11 Ma Getra-Kele basalts interbedded with fluvio-lacustrine sediments within the Chamo and Segen Basins [*Woldegabriel et al.*, 1991; *Ebinger et al.*, 1993]. The Getra-Kele Basalts are significantly thinner along the Amaro Horst, when present, and completely absent in the Gofa Province further west [*Ebinger et al.*, 2000]. A series of ~14 Ma trachytic-syenitic volcanic plugs, named the Mymo trachytes, intrude basement and overlying Amaro-Gamo basalts along the fault systems bounding the Chamo Basin [*Ebinger et al.*, 1993]. In the southern Chamo Basin, syn-rift fluvio-lacustrine sequences contain a proboscidean fossil dated between 17 and 15 Ma [*Woldegabriel et al.*, 1991]. Geochronological and biostratigraphic markers are, however, absent in the Galana Basin [*Ebinger et al.*, 1993].

3 Methodology

3.1 Sample collection and analyses

Thirteen Precambrian granitoid and gneissic basement samples from the Beto Basin, Gofa Province, and fifteen basement rocks from the Amaro Horst, between the Galana Basin to the east and Chamo and Segen Basins to the west, were collected to constrain the low-temperature thermal history of these areas of the Broadly Rifted Zone (BRZ) (Figures 2 and 3).

Field sampling in the Gofa Province was conducted along the northwest Beto Basin margin, with five samples collected along the base of the SE-dipping master fault scarp. An additional eight samples were collected in a vertical profile in the footwall of the ~NW-SE trending fault defining the southwest basin margin.

Sampling of the Amaro Horst consisted of two vertical transects up its eastern flanks, along the western margin of the Galana Basin. The first traverse consisted of nine samples between elevations of 1800 and 2420 m, which crossed a prominent east-dipping normal fault of unknown displacement between samples AM6-*1st tr* (2080 m) and AM7-*1st tr* (2000 m) [*Balestrieri et al*., 2016]. For ease of discussion, samples collected west, or above, this observed fault (AM2-*1st tr* to AM6-*1st tr*) are referred to herein as upper 1st traverse samples. Accordingly, samples collected east of, or below, the observed fault (AM7-*1st tr* to AM10-*1st tr*) are referred to as lower 1st traverse samples. Four additional samples were collected as part of the 2nd traverse between elevations of 1685 and 2004 m, 11 km to the north. Two more basement samples were collected on the western side of the Amaro Horst. AM1-*West* was sampled from the western base of the Amaro Horst, where it defines the eastern margin of Chamo Basin, at the same approximate latitude as the 1st traverse. AM1-*South* was sampled ~50 km SSW of the 1st traverse, at the base of the eastern Segen Basin margin.

3.2 Apatite fission track (AFT) and (U-Th-Sm)/He (AHe) methodologies

The AFT methodology is based on damage trails in apatite, called fission tracks, which form as a consequence of spontaneous fission of ^{238}U [*Fleischer et al.*, 1975; *Wagner and Van den Haute*, 1992]. Fission tracks are temperature sensitive between ~60 and ~110-120 °C, referred to as the partial annealing zone (PAZ), over geological timescales [*Gleadow and Duddy*, 1981; *Laslett et al*., 1987]. The compositional effect on fission track annealing kinetics can be assessed by a proxy measurement of the diameter of etched spontaneous track openings, parallel to the apatite crystallographic c-axis (Dpar) [*Sullivan and Parrish*, 1995; *Barbarand et al.*, 2003]. By combining fission track age and mean track length (MTL) data, the thermal history of a sample within the PAZ can be determined [*Gallagher*, 1995; *Ketcham*, 2005].

AHe thermochronology is based upon the production of ^{4}He during α-decay of ^{238}U, ^{235}U, ^{232}Th and ^{147}Sm [*Farley and Stockli*, 2002]. Volume diffusion of ^{4}He is a function of time, temperature, crystal size and accumulated radiation damage [*Farley*, 2000; *Reiners and Farley*, 2001; *Shuster et al.*, 2006]. In apatite, ^{4}He diffusion accelerates significantly above ~30 °C and nearly instantaneously above ~90 °C [*Reiners et al.*, 2005; *Reiners and Brandon*, 2006]. Within these temperatures, referred to as the apatite partial retention zone (AHe PRZ), ^{4}He is partially retained.

Combined AFT and AHe thermochronology provides a powerful tool for constraining the thermal history of apatite-bearing rocks between ~30-120 °C, approximately corresponding to the upper 2-5 km of the crust. Inverse modelling of AFT and AHe results (Section 6) allows for the identification of the most plausible time-temperature evolution recorded by those data [*Gallagher*, 1995]. The resulting thermal history reconstructions, in turn, provide important insights into the denudational and tectonic histories of geological terrains [*Kohn et al.*, 2005].

A comprehensive review of the AHe methodology and technical procedure used in this study can be found in *Gleadow et al.* [2015]. A detailed summary of the AFT and AHe analytical protocols are given in the footnotes of Tables 1 (AFT), 2 (Beto Basin AHe) and 3(Amaro Horst AHe). The thermal history modelling approach applied to these data, along with a discussion of the time-temperature reconstructions, are presented in Section 6.

Samples AM2-*1st tr*, AM1-*West* and AM4-*2nd tr* yielded insufficient apatite grains for AHe experimentation, while AHe analysis was not attempted on samples GR5 to 10. For samples that did yield suitable grains for AHe analysis, an alpha ejection correction (F_T) was applied to calculate a corrected age (Tables 2 & 3), as suggested by *Farley et al.* [1996]. However, it has been shown that for samples with protracted thermal histories in the PRZ, as is the case for slowly cooled basement terranes, volume diffusion is the dominant mechanism governing He loss. Thus, the application of F_T in these cases may result in inaccurately old ages [*Meesters and Dunai*, 2002; *Danišik et al.*, 2008]. Therefore, all AHe data discussed in the text and displayed in figures are uncorrected ages. The effects of alpha ejection were still accounted for during inverse thermal history modelling, discussed in Section 6.

AHe data were complemented by published AFT analyses [*Philippon et al.*, 2014; *Balestrieri et al.*, 2016]. However, for Beto Basin NW margin and Amaro Horst 2nd traverse samples, confined track length measurements were few or, in many cases non-existent, preventing statistically robust thermal history modelling to be performed. Therefore, new confined track measurements were carried out on these samples after being irradiated by ^{252}Cf for 60 minutes at the University of Melbourne, increasing the number of visible confined tracks and improving MTL statistics.

4 Results

Newly acquired AFT confined track data are presented in Table 1, and Figures 2 and 3. AHe results from the Beto Basin and Amaro Horst are presented in Tables 2 and 3, respectively. All ages are reported to one decimal place in the tables but rounded to whole numbers in the text, except for ages with 1σ errors < 1 Ma. Single grain AHe ages are reported with a conservative 6.2% (1σ) analytical error. Results are discussed by methodology in order of decreasing temperature sensitivities. Within these subsections, data are grouped by regions of shared thermal histories (Beto Basin and Amaro Horst), as determined by *Philippon et al.* [2014] and *Balestrieri et al.* [2016].

4.1 Apatite fission track analyses

4.1.1 Beto Basin

Precambrian basement rocks from the southwest margin of the Beto Basin (AFT ages between 76 ± 5 Ma to 59 ± 8 Ma) yield intermediate to long MTL (12.1 to 13.4 μm) and small to moderate standard deviations (0.95 to 1.90 μm) that show no correlation with Dpar (2.3-3.4 μm) (Table 1). By contrast, samples from the Beto Basin-bounding fault scarp

produced MTL that range between 11.2 and 12.8 μm, with large standard deviations (2.17 to 3.57 μm). Dpar measurements (2.1-2.5 μm) exhibit a positive correlation to MTL and slightly negative correlation to AFT age.

4.1.2 Amaro Horst

MTL measurements from the Amaro Horst 1st traverse are moderate to long (11.0 to 13.8 μm) with intermediate standard deviations (1.26 to 2.63 μm). These data exhibit a negative correlation to elevation (Figure 3) that, like AFT age-elevation relationships, are consistent with higher samples being less thermally rejuvenated with respect to the AFT system. This pattern is slightly disturbed by a "step" in MTL and AFT ages corresponding to where *Balestrieri et al.* [2016] observed a normal fault with significant, but unknown offset. AM1-*South* yields a MTL of 12.9 μm with a standard deviation of 1.30 μm, consistent with other 1st traverse samples.

By contrast, samples from the Amaro Host 2nd traverse yield MTL data that are longer (12.7-13.4 μm) than their 1st traverse counterparts but exhibit similarly moderate standard deviations (2.07-2.57 μm). These data are consistent with their much younger AFT ages (12 ± 3 and 6.8 ± 0.7 Ma), suggesting a greater degree and possibly more recent thermal resetting. Accordingly, the number of observed confined track length measurements for 2nd traverse samples are low, even after ^{252}Cf irradiation. Despite only five confined track measurements being obtained, sample AM4-*2nd tr* yields a MTL of 11.9 μm with a standard deviation of 2.28 μm that is in agreement with AM2-*2nd tr* and AM5-*2nd tr*. Conversely, AM1-*2nd tr* (6 confined track measurements) yields a markedly shorter MTL (9.4 μm) with very large standard deviation (3.70 μm), at odds with other samples in the traverse. Thus, AM1-*2nd tr* is treated as an outlier and omitted from further discussion.

4.2 Apatite (U-Th-Sm)/He analyses

AHe analyses from both the Beto Basin and Amaro Horst regions exhibit significant age dispersion. A wide range of crystallographic and compositional characteristics have been shown to affect He diffusion in apatite, at times producing intra-sample He age dispersion greater than 50% [*Wolfe and Stockli*, 2010; *Wildman et al.*, 2016]. Of particular concern to this study, are grain size, morphology and accumulated radiation damage, all of which are considered during data interpretation and thermal history modelling (Figure 4). The potential effect of grain size on He diffusion is assessed by comparing AHe ages versus equivalent spherical radius (R_s; $R_s = [3 \bullet R \bullet L]/[2 \bullet \{R+L\}]$), allowing for the comparison of 0, 1 and 2 termination grains. Radiation damage modified He diffusion effects are assessed by using effective uranium concentration (eU; eU = U + 0.235 x Th) as a proxy for α-radiation damage, which takes into account the decay rate and abundance of radiogenic parent elements.

4.2.1 Beto Basin

AHe ages from the southwestern margin of the Beto Basin range from 31 ± 2 Ma to 10.7 ± 0.7 Ma and generally show no correlation to grain size or morphology. Of these, six 2T grains yield ages between 39 ± 2 Ma and 13.1 ± 0.8 Ma. Sample GR11 (27 ± 2 to 10.7 ± 0.7 Ma; 5 grains) however, shows a strong positive correlation to eU content (Figure 4).

Apatite He analyses from the Beto Basin-bounding fault scarp yield ages between 2.7 ± 0.2 Ma and 90 ± 6 Ma, exhibiting a general trend of decreasing age towards the northeast (Table 2). Only one 2T grain was obtained (sample GR12) and yields an AHe age of 10.6 ± 0.7 Ma. Apart from GR13 (5 grains; 90 ± 6 to 5.3 ± 0.3 Ma), rocks from the northwest margin exhibit far less intra-sample AHe age dispersion (13.4 ± 0.8 to 2.7 ± 0.2 Ma). Apatites from GR13 appear to show a strong correlation between age and morphology, with its one 1T grain (90 ± 6 Ma) yielding an AHe age more than double the next oldest. The remaining grains (all 0T; 40 ± 3 to 5.3 ± 0.3 Ma) exhibit positive age-grain size correlations.

4.2.1 Amaro Horst

Single grain AHe results from the Amaro Horst 1st traverse range from 5.5 ± 0.3 Ma to 119 ± 7 Ma. Upper 1st traverse samples show a general decrease in age and dispersion with elevation (Table 3), contrary to the AFT age-elevation trend for these samples (Table 1) and opposite of what might be expected for vertical transects [e.g. *Fitzgerald et al.*, 2006]. In general, intra-sample single grain AHe age variation does not display any clear relationships with morphology, grain size or eU concentration. The exceptions being AM6-*1sttr* (12.2 ± 0.8 to 119 ± 7 Ma), showing a positive age-grain size correlation, and AM4-*1sttr* (38 ± 2 to 53 ± 3 Ma), whose AHe ages display a slight correlation with eU content. The sole 2T grain analysed from upper 1st traverse samples (AM3-*1sttr*) records an AHe age of 26 ± 2 Ma.

Lower 1st traverse samples, on the other hand, do not show a clear age-elevation relationship (Table 3). Single grain ages are more dispersed than their 1st traverse counterparts, ranging from 146 ± 9 Ma to 5.5 ± 0.3 Ma. Dispersion in the three 2T grains analysed from lower 1st traverse samples is reduced, but apparent (70 ± 4 to 7.2 ± 0.4 Ma). In the few instances where samples do exhibit a strong relationship with a certain parameter, the trend is often the opposite of what might be expected. For example, sample AM8-*1sttr* exhibits negative correlations between AHe age and both grainsize and eU content. AM1-South, on the other hand, yields predominantly older single grain ages (3 grains; 68 ± 4 to 56 ± 4 Ma), apart from a very young 0T grain (5.4 ± 0.3 Ma).

Samples from the Amaro Horst 2nd traverse yield younger, far less dispersed AHe ages between 31 ± 2 Ma to 2.8 ± 0.2 Ma that show no relationship to elevation (Table 3). 2T AHe results (4 grains) exhibit very little age dispersion and range from 5.2 ± 0.3 Ma to 2.9 ± 0.2 Ma. Sample AM5-*2ndtr* (3 grains; 22 ± 1 to 3.5 ± 0.2 Ma) shows a strong correlation with eU content (Figure 5). Apatites from sample AM1-*2ndtr* (4 grains; 31 ± 2 to 4.3 ± 0.3 Ma) exhibit negative age-eU and age-R_s trends.

4.3 Apatite (U-Th-Sm)/He age dispersion

Single grain AHe ages obtained in this study exhibit complex relationships with accumulated radiation damage, grain size and morphology (Figure 4). Intra-sample single grain AHe age variation relationships to eU content and R_s often differ from the positive correlations that may be expected for relatively slowly cooled rocks [*Reiners and Farley*, 2001; *Flowers et al.*, 2009]. These are likely the result of the competing effects of grain size and radiation damage, decoupling the expected correlation [*Brown et al.*, 2013; *Wildman et al.*, 2016]. These complications are perhaps also compounded by other unquantified factors such as U, Th, and Sm zonation [*Flowers and Kelley*, 2011] and apatite chemistry [*Gautheron et al.*, 2013; *Mbongo Djimbi et al.*, 2015]. The analysis of fragmented apatite grains likely further convolutes these relationships by producing ages that differ from their whole grain equivalents [*Wildman et al.*, 2016]. One termination (1T) fragments can produce older or younger ages than the whole grain age, while no termination (0T) grains are most likely to yield older ages [*Brown et al.*, 2013].

Similar complex age dispersion patterns have been observed in previous AHe studies from slowly cooled terranes [e.g. *Flowers et al.*, 2007; *Kohn et al.*, 2009]. Despite these complications, general relationships between the degree of single grain AHe age dispersion and the thermal history of a sample or group of samples have been identified. For instance, the effects of radiation damage and grain size on He diffusion has been shown to become more pronounced during thermal histories characterized by slow cooling, prolonged residence in the AHe PRZ or protracted reheating [*Fitzgerald et al.*, 2006; *Brown et al.*, 2013]. Whereas, datasets with low inter-aliquot age dispersion, despite variation in eU content and grain size, are indicative of rapid cooling or complete resetting during reheating [*Flowers and Kelley*, 2011]. Thus, the degree of age dispersion exhibited by a sample, or group of samples which share a similar thermal evolution, can be used to characterise their cooling history.

Brown et al. [2013] suggested quantifying intra-sample dispersion by dividing the range of ages (i.e. *maximum age – minimum age*) by the mean. The calculated dispersion [%] was then used as a simple way to apply a value to the degree of intra-sample age variance experienced by a sample. However, for comparison of age dispersion between different groups of samples, with each group consisting of samples that share a similar thermal history, the statistical measure of dispersion suggested by *Brown et al.* [2013] is inappropriate because datasets with lower means will, by definition, yield higher dispersion percentages. In other words, AHe data from a basement block that experienced rapid uplift and cooling in the Neogene would be considered significantly more dispersed than AHe results from rocks that experienced the exact same duration and rate of uplift and cooling in the Cretaceous, despite yielding the same spread in, albeit older, ages. Instead, we use the interquartile range (IQR):

$$IQR = Q_3 - Q_1$$

where Q_1 and Q_3 are the first and third quartiles, respectively. The IQR is a computationally simplistic robust scale estimator and, thus, resistant to outliers. Moreover, the IQR statistic

does not assume a symmetric data distribution [*Rousseeuw and Croux*, 1993] and is independent of a dataset's mean. Assuming that the nature of single grain AHe age dispersion is characteristic of a dataset's thermal history [*Fitzgerald et al.*, 2006; *Flowers and Kelley*, 2011; *Brown et al.*, 2013], the use of IQR allows for a first order comparison of the type of cooling history experienced by different samples, or groups of samples, independent of timing. For example, a group of samples that experienced rapid cooling through the AHe PRZ or complete resetting during reheating should record low inter-aliquot age dispersion [*Flowers and Kelley*, 2011] and, thus, a low IQR. Whereas, a group of rocks that experienced slow cooling, prolonged residence in the AHe PRZ or protracted reheating should record broad single grain age variance [*Fitzgerald et al.*, 2006; *Brown et al.*, 2013] and a large IQR.

5 Discussion

AFT and AHe analyses from the Beto Basin and Amaro Horst yield important constraints on the thermal evolution of the BRZ of southern Ethiopia. The relationship between these two data sets is illustrated in Figure 5, where AFT ages are plotted against MTL data for groups of samples that have shared very similar thermal histories as determined in previous low-temperature thermochronology investigations [*Philippon et al.*, 2014; *Balestrieri et al.*, 2016]. These so-called boomerang plots usefully illustrate multi-stage thermal histories for sets of samples that have cooled from different paleotemperatures during a later period of cooling [*Green et al.*, 1989; *Gallagher and Brown*, 1997]. Samples that record an early period of pronounced cooling, but were negligibly affected by subsequent reheating and cooling, will yield older ages with relatively long MTL (> 14 μm). By contrast, samples that cooled from paleotemperatures greater than ~110-120 °C during the final cooling stage will record relatively long MTL (> 14 μm) and young AFT ages, which approximate the timing of later cooling. Alternatively, samples that cooled from temperatures within the PAZ (~110-60 °C) during the final cooling episode will yield intermediate "mixed" AFT ages with shortened MTL.

Samples from the southwest margin of the Beto Basin form the descending portion of a boomerang curve (Figure 5), characteristic of an early period of pronounced cooling, such as Late Cretaceous-earliest Paleogene denudational cooling of the Anza Rift margins recorded regionally [e.g. *Foster and Gleadow*, 1992, 1993, 1996; *Torres Acosta et al.*, 2015], followed by reheating into and/or prolonged residence in the PAZ. Subsequent exhumation and cooling were then required to expose samples with substantially annealed MTL to the surface. This is consistent with their Oligocene-Miocene single grain AHe ages, which are moderately skewed towards younger ages and have an intermediate IQR of 14.1. Samples collected from the footwall of the Beto Basin-bounding master fault, by contrast, form the ascending portion of a boomerang curve, suggesting these samples cooled from paleotemperatures in the upper PAZ during this final cooling phase. This is reflected in the limited spread in AHe data and correspondingly low IQR (5.3). By projecting the boomerang curve to longer MTL, we estimate that this later cooling phase likely occurred sometime during the Miocene-Pliocene, consistent with 18 of 22 single grain AHe results (13.4 ± 0.8 to 2.7 ± 0.2 Ma).

AFT analyses of Amaro Horst 1st traverse samples record little late Cenozoic cooling, as indicated by the corresponding boomerang plot and large IQR (38.0) of the corresponding AHe data. Instead, these data form the ascending portion of a boomerang trend that curves towards relatively long MTL samples, AM4-*1st tr* (75 ± 4 Ma; 13.8 μm) and AM10-*1st tr* (73 ± 7 Ma; 13.8 μm). The slightly younger ages and shorter MTL of samples AM6-*1st tr* (70 ± 7 Ma; 12.8 μm) and AM1-*South* (66 ± 4 Ma; 12.9 μm) suggest that these samples may form the very beginning of a younger boomerang curve which extends towards a subsequent period of late Cenozoic cooling (light grey arrow in Figure 5). This is in strong accordance with Amaro Horst 1st traverse AHe analyses, 32 of 34 of which yield latest Cretaceous-Miocene ages (70 ± 4 to 5.5 ± 0.3 Ma).

Late Cenozoic cooling hinted at by the spread of Amaro Horst 1st traverse samples is more-clearly evident in the age-MTL plot of 2nd traverse samples. Here, AFT data distinctly form the ascending arm of a boomerang curve, which extends towards long MTL's (>14 μm). The substantially younger AFT ages (12 ± 3 to 6.8 ± 0.7 Ma) and relatively longer MTL (11.9-13.4 μm) suggest that these samples cooled from elevated temperatures within the PAZ during later Miocene-Pliocene cooling. This is supported by 2nd traverse AHe data, which exhibit very low dispersion (12 grains; IQR = 1.8) and skew towards latest Miocene-Pliocene ages (ten single grain ages between 6.7 ± 0.4 Ma to 3.6 ± 0.2 Ma).

6 Thermal History Modelling

In order to quantify thermal histories for the Beto Basin and Amaro Horst of the BRZ, AFT and AHe data were inversely modelled using *QTQt* [*Gallagher*, 2012], with the multi-compositional fission track annealing model of *Ketcham et al.* [2007a] (Figure 6). Confined fission track lengths were normalised for annealing and etching anisotropy using the c-axis projection method [*Ketcham et al.*, 2007b]. Differences in AHe grain-size were accounted for by using the alpha ejection correction (F_T) [*Farley et al.*, 1996]. Radiation damage accumulation and annealing models were employed for modelling of AHe data [*Gautheron et al.*, 2009] to account for differences in radiation-modified diffusion kinetics recorded by age-eU relationships. However, these models are unable to account for all known sources of intrasample ZHe and AHe age dispersion, such as chemical zonation [*Guenthner et al.*, 2013] and apatite composition [*Gautheron et al.*, 2013]. Therefore, during modelling, *QTQt* was allowed to resample the He error for single grain ages, effectively reducing their influence on determining thermal histories compared to data from the AFT system, whose thermal annealing kinetics are better understood [*Gallagher*, 2012]. For samples with fragmented AHe grains, only 1- and 2-termination grains were modelled in *QTQt*, due to the current implementation of the *Brown et al.* [2013] fragmentation model's inability to process 0-termination grains.

Samples were initially modelled individually (e.g. AM1-*South*), unless they had a relatively low number of confined track measurements (< 60). A constraint was applied to all models, requiring samples to be at surface temperatures (20 ± 10 C) by the present-day. Samples then underwent thermal history modelling again, with the addition of a second time-temperature

constraint. This second constraint corresponds to the emplacement of the Gamo Amaro basalts (45-35 Ma) [*Ebinger et al.*, 1993] above Precambrian basement in the Beto Basin and Amaro Horst regions, requiring samples to be at near-surface temperatures during that time. The temperature range for this constraint varied between samples, and was determined using the difference in elevation between it and the base of the overlying Gamo Amaro basalt and the average paleogeothermal gradient of Proterozoic mobile belts in East Africa [30 °C /km; *Nyblade*, 1990]. This constraint was omitted from samples from the Amaro Horst 2nd traverse, as any volcanic rocks that may have once overlain those rocks have since been eroded away, preventing estimation of paleo-depths. Thermal history models for individual samples not included in Figure 6 are presented in the Supporting Information (Figures S1 and S2). Where possible, samples were then modelled together as vertical profiles to improve modelling statistics. Samples with low confined track measurement (< 60) were included in vertical transect models, as they were given little weight in determining probable time-temperature paths compared to more statistically robust data in their group. Vertical transect thermal history modelling was performed for samples from the Beto Basin southwest margin (GR4-11), upper Amaro Horst 1st traverse (AM2-*1st tr*- AM6-*1st tr*), lower Amaro Horst 1st traverse (AM7-*1st tr*- AM10-*1st tr*) and the Amaro Horst 2nd traverse (AM1-*2nd tr*- AM5-*2nd tr*).

6.1 Cretaceous-early Paleogene Anza Rifting and Eocene-early Miocene magmatism

Thermal history models from both the Beto Basin southwest margin and the Amaro Horst 1st traverse record an initial period of pronounced Late Cretaceous-early Paleogene cooling, beginning between ~120-90 Ma and reaching near-surface temperatures by the late Eocene (45-35 Ma). Thermal history models for samples GR3, GR4, GR12, GR14 and the Amaro Horst 2nd traverse are not constrained prior to Eocene time due to the total, or near-total, resetting of AFT and AHe data during subsequent late Paleogene reheating. However, their proximity to samples whose thermal history models extend back to Cretaceous times and the lack of intervening pre-EARS structures allows for the assumption that these also experienced protracted Late Cretaceous-Eocene cooling. Thermal history models from the Beto Basin southwest margin and Amaro Horst 1st traverse suggest that during the Late Cretaceous-Eocene they experienced an initial period of rapid cooling (2.5-5 °C/Ma), followed by a transition to protracted cooling (0.33-1.67 °C/Ma) sometime between 90-70 Ma.

The presence of a top basement erosional unconformity and large decreases in paleotemperature (~80-90 °C), as indicated by t-T reconstructions, are consistent with erosional denudation as the mechanism for observed cooling. A similar period of denudational cooling, both in timing and character, has been observed in low-temperature thermochronology studies performed throughout much of East Africa [e.g. *Foster and Gleadow*, 1992, 1993, 1996; *Noble et al.*, 1997; *Torres Acosta et al.*, 2015; *Boone et al.*, 2018a, b]. This pervasive period of cooling has been interpreted as recording denudation of the Anza rift margin and adjacent hinterlands during the development of the NW-SE trending, Cretaceous-early Paleogene graben [e.g. *Foster and Gleadow*, 1992].

Between 45 Ma and 35 Ma, the BRZ was uniformly covered by voluminous [2000-2300 km^3; *Ebinger et al*., 1993] Amaro Gamo basaltic flows, marking the earliest manifestation of EARS-related volcanism in East Africa. This is recorded in all thermal history models presented in this study by a transition to a period of marked reheating ca. 45 Ma. Time-temperature reconstructions suggest that basement samples from the Beto Basin and the Amaro Horst 1st and 2nd traverses experienced an increase in temperature of between ~45-60 °C by the early Miocene. The regularity in timing, rate and magnitude of observed reheating in samples across the BRZ suggest localized heating mechanisms, such as conductive heat flow from magma intrusions or lava flows, were insignificant with respect to AFT and AHe rejuvenation. Instead, regional Eocene-early Miocene reheating is best explained by burial beneath a ~1.5-2 km pile of Gamo Amaro basalt (using a paleogeothermal gradient of 30 °C/km), similar to thicknesses preserved in the eroded western Beto Basin margin [up to 1100 m; *Balestrieri et al*., 2016]. This is a maximum estimate, however, as an increase in basal heat flow following the impingement of a mantle plume beneath the region ca. 45 Ma may have also contributed to the observed reheating. By comparison, the thermal history model for sample AM1-South records very little, if any (up to 10 °C), late Paleogene reheating, consistent with its retention of Cretaceous AFT and AHe ages. This suggests that the thickness of Gamo Amaro basalt flows decreased substantially towards the south, likely reaching no more than 300 m in the Segen Basin area.

6.2 Miocene-Recent development of the BRZ

Beginning in the early Miocene, thermal history models indicate that the Beto Basin margins and the Amaro Horst experienced a phase of pronounced cooling, reaching near surface temperatures by the present day. This coincided with an important period of significant normal faulting, basin formation, and rift-shoulder uplift throughout much of southern Ethiopia in relation to the Miocene-Recent development of the BRZ [e.g. *Ebinger et al*.,1993; *Bonini et al*., 2005; *Pik et al*., 2008; *Philippon et al*., 2014]. Upper crustal deformation was accompanied by continued, albeit less extensive, rift magmatism (18-11 Ma Getra-Kele basalts and 14 Ma Mymo trachytes), restricted to the eastern BRZ [*Ebinger et al*., 1993; *Ebinger et al*., 2000]. However, observed Neogene-Recent magmatic intrusions and eruptive centres in the Amaro Horst region are restricted to the Chamo and Segen Basins [*Levitte et al*., 1974; *Ebinger et al*., 1993].

In certain cases, the emplacement of magmatic intrusions or lava flows can reheat surrounding or underlying country rock to temperatures adequate to rejuvenate low-temperature thermochronometers [e.g. *Tagami and Shimada*, 1996; *Reiners et al*., 2005]. However, reheating patterns detected by low-temperature thermochronology in relation to transitory heating mechanisms, like intrusions, lava flows, hydrothermal fluids, or heated groundwater, are highly localised, generally restricted to the centimeter- to meter-scale [e.g. *Mitchell and Reiners*, 2003; *Ehlers*, 2005; *Reiners et al*., 2007], and characterised by significantly reset samples interspersed with, and in close proximity to, unaffected samples [e.g. *Gallagher et al*., 1994; *Gunnell et al*., 2003; *Seiler et al*., 2009; *Boone et al*., 2016]. The lack of Neogene-Recent magmatism in the western BRZ and absence of dykes or volcanic edifices within the Galana Basin or along the eastern Amaro Horst [*Levitte et al*., 1974;

Ebinger et al., 1993], thus, suggest that AFT and AHe data were likely unaffected by the region's limited Neogene magmatic history. Present-day high heat flow measurements in nearby Turkana [*Morley et al.*, 1999b] and continued, albeit less extensive, volcanic activity in the southern MER [*Zanettin et al.*, 1978; *Corti*, 2009] also argue against a Neogene-Quaternary decrease in geothermal gradient having caused the observed cooling.

Instead, the highly eroded nature of the volcanic sequences capping the Beto Basin margins and Amaro Horst [*Levitte et al*.,1974; *Ebinger et al*.,1993; *Balestrieri et al*., 2016] suggest that observed Miocene-Recent cooling likely reflects rift shoulder uplift and denudation in response to normal faulting. Such a scenario is further supported by basin stratigraphy, where exposed.

6.2.1 Miocene-Recent tectono-thermal evolution of the Beto Basin

Thermal history models from samples in the footwall of the southwest Beto Basin margin-defining fault and the southernmost samples (GR12 and GR3) from the basin's northwest shoulder indicate that these rocks began to experience rapid cooling (~6-10 °C/Ma) in the early Miocene (20-17 Ma). Circa 14 Ma, cooling rates of the southwest Beto margin appear to have substantially slowed (~0.7 °C/Ma), perhaps indicating a marked decrease or cessation of any vertical component of displacement accommodated along the southwestern margin-bounding fault. Rapid cooling along the southern NW basin margin (samples GR12 and GR3) however, continued unabated until Recent times. Coeval with the observed change in cooling rates along the Beto southwest margin, samples from the northern half of the northwest basin margin (GR2 and GR14) began to cool, possibly reflecting the initiation of a new fault segment northeast of the town of Beto (Figure 2). At first, cooling rates were gradual (~2.5-3 °C/Ma). Around 8-6 Ma however, cooling rates along the northern, NW margin substantially increased (~9-12.5 °C/Ma).

Such a north-eastward migration of strain along the NW margin is consistent with the triangular geometry and northward narrowing of the Beto Basin, as well as the local, southward increase in the amount of extension in the Gofa province, which collectively imply large-scale counter clockwise rotation [*Philippon et al.*, 2014]. This model also predicts that the ~NW-SE trending faults delimiting the southwest margins of the Gofa Province basins must have acted as dextral transfer zones during large-scale rotation. Low-temperature thermochronology data, indicating a concurrent north-eastward migration of strain along the Beto Basin's NW margin and cessation or significant decrease in footwall denudation along its SW margin ca. 14 Ma, are consistent with this scenario and may indicate the onset of large-scale counter clockwise rotation.

6.2.2 Amaro Horst Miocene-Recent thermal evolution and the development of the Chamo and Galana Basins

As the Amaro Horst is bound by both E- and W-dipping normal fault arrays, its uplift history undoubtedly reflects the structural evolution of both fault systems. However, the westward

tilt of the Amaro block, which reaches its highest elevations along its much steeper eastern margin, suggests that footwall uplift has been greatest along the east-dipping Galana Basin-bounding fault system. This asymmetry is further reflected in the contrasting geometries of the surrounding basins: syn-rift infill in the Galana Basin is thought to expand significantly into the western basin-bounding fault system and reach thicknesses of > 4 km, while the eastern margin of the shallower (< 2 km) Chamo Basin is defined by a series of gradually stepping, small-throw faults [*Ebinger et al*., 1993]. Furthermore, sample AM1-West, the sole basement sample from the western margin of the northern Amaro Horst (Figure 2), retains a very old AFT age [103 ± 25 Ma; *Balestrieri et al*., 2016], suggesting Neogene-Recent footwall uplift along the eastern margin of the Chamo Basin was insufficient to exhume rocks from within the AFT PAZ. These observations suggest that the Miocene-Recent cooling histories of 1st and 2nd traverse samples, collected along the eastern Amaro Horst margin, were primarily controlled by the structural evolution of the E-dipping normal fault system bounding the proximal Galana Basin.

Upper 1st traverse (AM2- to AM6-1st tr) and 2nd traverse samples record a broadly coeval onset of pronounced cooling ca. 20-18 Ma, suggesting that footwall uplift in response to Galana Basin formation had begun by that time. *Ebinger et al*. [1993] invoked a similar early Miocene onset of Galana Basin formation on the basis of stratigraphic relationships. A broadly concurrent onset of Chamo Basin formation further west is also supported by the presence of syn-rift fluvio-lacustrine deposits which contain early Miocene fauna [17-15 Ma; *Woldegabriel et al*., 1991]. Thermal history models suggest that lower 1st traverse samples however, did not transition to a period of cooling until ~ 13 Ma, by which time the difference in paleotemperatures between the lowermost upper 1st traverse sample (AM6-1st) and the uppermost lower 1st traverse sample (AM7-1st) was as much as 45 °C (Figure 6), despite their present-day proximity. One explanation for this is that the intervening normal fault accommodated a significant amount of throw (perhaps as much as 1 km) between ~18 Ma and 13 Ma, decoupling upper and lower traverse thermal histories. According to such a scenario, the continued reheating of lower 1st traverse samples into the middle Miocene would have resulted from burial beneath early syn-rift Galana Basin infill.

Circa 13 Ma, lower 1st traverse samples (AM7- to AM2-1st tr) began a pronounced period of cooling (~4.5 °C/Ma) that continued into the Quaternary. At the same time, upper 1st traverse basement samples transitioned to a period of substantially reduced cooling (~0.5 °C/Ma) or thermal stability that has continued until the present day. This marked change in southern Amaro Horst cooling history is interpreted as recording an eastward migration of strain in the southern Galana Basin, subsequently accommodated on a fault or faults basin-wards of the lower 1st traverse samples. Consequently, the location of lower 1st traverse samples in the more proximal footwall of the newly active fault resulted in their rapid uplift and exhumation. By contrast, the more distal position of upper 1st traverse samples relative to the newly active fault resulted in reduced uplift and exhumation rates [*Barnett et al.,* 1987]. A similar basin-wards migration of strain has been documented in the neighbouring Chamo Basin, where the locus of extension, as well as volcanism, shifted to the foot of the western-bounding border fault by Pliocene-Recent time [*Ebinger et al*., 1993].

The thermal history model of sample AM1-South suggests that this segment of the Segen Basin's eastern margin experienced no more than 20 °C of cooling, equivalent to a maximum of ~0.7 km of denudation, during Miocene to Recent times. However, this period of cooling is poorly constrained by its Cretaceous AFT and three Cretaceous-Paleogene AHe aliquot ages. Only one apatite grain (0T) from AM1-South yielded a Neogene age (5.4 ± 0.3 Ma). Despite this, a middle Miocene onset of Segen Basin development is consistent with the stratigraphic relationship of syn-rift lacustrine mudstones that onlap ~17-12 Ma phonolites within the basin [*Ebinger et al.*, 2000].

6.3 Comparison of newly acquired and previous thermal history models

In general, time-temperature reconstructions presented here are broadly consistent with the low-temperature thermal evolutions previously suggested for the Beto Basin and Amaro Horst regions [*Philippon et al.*, 2014; *Balestrieri et al*., 2016]. The most important difference between new and previous thermal history models concerns the onset of Miocene cooling for Beto Basin NW margin and Amaro Horst samples. Thermal history models presented herein indicate a coeval early Miocene (~20-17 Ma) onset of cooling in these regions, significantly earlier than the middle-late Miocene initiation (14-10 Ma Beto Basin, 10-8 Ma Amaro Horst) suggested previously [*Balestrieri et al*., 2016].

In certain cases, this difference can be attributed to the addition of AHe analyses during thermal history modelling. For example, the retention of Cretaceous AFT ages in Amaro Horst 1st traverse samples indicate that these rocks did not cool through the AFT PAZ (~120-60 °C) during Miocene-Recent times. Therefore, their AFT data alone poorly constrain the Miocene onset of rift-related denudation. The addition of data from the lower temperature AHe system (~90-30 °C) provides improved resolution over the range of temperatures corresponding to the maximum paleotemperatures experienced by Amaro Horst 1st traverse samples prior to Miocene cooling (~70-90 °C, Figure 6).

The robustness of thermal history models for samples from the Beto Basin NW margin and Amaro Horst 2nd traverse also improved due to increased low-temperature resolution provided by the addition of AHe analyses. However, their earlier onset of Miocene cooling indicated by thermal history models in this study is attributed to their greatly improved confined fission track measurement statistics, resulting from supplemental analysis using the ^{252}Cf irradiation method. The number of confined tracks available for measurement improved substantially (by between 6 and 3750%). The most extreme example being sample GR2, whose number of confined tracks measurements increased from 2 to 77. The application of the ^{252}Cf irradiation method to samples AM5-2nd tr, AM4-2nd tr, and AM1-2nd tr, which previously had no confined track length measurements, resulted in 76, 5, and 6 measurements, respectively. In all cases, MTL decreased from relatively long lengths [15.2-11.9 μm; *Balestrieri et al*., 2016] to more moderate values (13.4-11.2 μm), indicative of more prolonged residence in the AFT PAZ. Consequently, new thermal history results suggest that

these rocks began cooling through the PAZ earlier than previously suggested, albeit from similar maximum paleotemperatures (~120-110 °C).

7 Possible insights into normal fault array evolution as revealed by low-temperature thermochronology

Low-temperature thermochronology of the Beto and Galana basin margins reveal high time-temperature resolution, polyphase cooling histories, which provide previously unavailable insights into along-strike denudational cooling trends. Intriguingly, the contrasting along-strike footwall cooling histories of the Beto and Galana margins appear to reflect the disparate structural geometries of their basin-bounding fault systems. This is perhaps unsurprising because as normal fault systems grow and accumulate displacement, their footwalls experience predictable uplift and denudational histories [*Harbor*, 1997; *Densmore et al.*, 2007] that results in the development of expected patterns of topography [*Densmore et al.*, 2004]. Indeed, other authors have exploited these fault growth-denudation relationships by using along-strike cooling history patterns, as recorded by low-temperature thermochronology age spectra, to investigate the mechanisms by which normal fault systems have evolved [*Curry et al.*, 2016; *Mortimer et al.*, 2016; *Brown et al.*, 2017].
Here, we present a conceptual model whereby along-strike variations in inversely modelled thermal histories, generated using AFT and AHe data, may be utilised to elucidate normal fault array growth (Figure 7). Similar to previous approaches [*Curry et al.*, 2016; *Mortimer et al.*, 2016; *Brown et al.*, 2017], which used variations in age spectra alone to investigate fault system evolution, it is the along-strike difference in the onset of footwall cooling that is the primary diagnostic indicator for distinguishing between end-member fault growth models. However, unlike previous models, this approach both accounts for compositional, morphological and radiation damage effects on AFT and AHe data by incorporating annealing and diffusion models during thermal history modelling (Section 6), as well as allows for the estimation of displacement accumulation trends at various stages of fault evolution (Figure 7). Importantly, this approach requires that the amount of footwall exhumation associated with faulting must be sufficient to exhume rocks from within or through the temperature sensitivities of the AFT and AHe systems for thermal history models to be able to constrain such spatio-temporal cooling variations. Moreover, the ability of combined AFT and AHe low-temperature thermochronology to resolve small differences in cooling behaviour between samples is limited by the quality of data, the accuracy of the AFT annealing and AHe diffusion kinetic models used to produce time-temperature reconstructions [*Flowers et al.*, 2015], the biases inherent in the inverse modelling approach of the thermal history modelling software employed [*Vermeesch and Tian*, 2014] and the modelling parameters [*Gallagher and Ketcham*, 2018]. Additionally, care must be taken when interpreting along-strike variations in basin margin cooling histories, as expected relationship between normal fault system growth and footwall exhumation can be complicated by natural factors, such as differences in fault rock elasticity (i.e. Young's modulus) and fault strength heterogeneities [*Cowie and Shipton*, 1998] that may affect fault array evolution, or variables which may influence basin margin denudation, like the efficacy of surface processes [*Densmore et al.*, 2004; *Densmore and Guidon*, 2005] and the existence

of antecedent topography [*Densmore et al.*, 2009]. Nevertheless, available low-temperature thermochronology data and thermal history models from the Beto and Galana Basin margins are consistent with our current understanding of the structural architecture of these basins. Further work, however, will be required to explicitly test the reproducibility and resolution of such an approach.

The fault system bounding the Beto half-graben is comprised of a series of ~SW-NE striking faults partitioned by shorter, ~NW-SE trending fault segments [*Philippon et al*., 2014]. Such a configuration is often associated with fault systems which have evolved via the elongation and eventual linkage of individual fault segments [e.g. *Soliva and Benedicto*, 2004], sometimes referred to as the segment growth and linkage model [*Kim and Sanderson*, 2005; *Fossen and Rotevatn*, 2016]. Significant along-strike spatial and temporal variations exhibited in the Beto Basin footwall are consistent with such a fault evolution (Figure 7). Thermal history models indicate that rift-related denudation first began in the faulted margins bounding the southwest end of the basin around 18 Ma. The concurrent initiation of cooling and similar cooling behaviour exhibited by samples GR3 and GR12 suggest that the corresponding portions of the southern Beto basin-bounding fault were mechanically linked prior to the accumulation of significant displacement and footwall uplift, resulting in a shared cooling history. Only later, at ~14 Ma did denudational cooling of the northern NW margin (samples GR2 and 14) begin. By then, samples GR3 and GR12 had experienced a significant amount of cooling (~10 °C). The delayed onset of cooling in the northern Beto Basin NW margin is interpreted to represent the formation of a new, initially independent fault segment to the north of Beto township. In this scenario, the rapid increase in cooling rates observed for samples GR2 and GR14 ca. 8-6 Ma reflect increased late Miocene-Recent displacement rates along the northern fault segment following its interaction and linkage to the already established fault system further south (samples GR3, 12 and 13), resulting in the development of a through-going boundary fault system along the Beto Basin NW margin. By this time, southern NW margin samples (GR12 and 3) had cooled ~50 °C (equivalent to ~1.5-2 km of exhumation). A similarly disjointed, along-strike cooling history in the Livingstone Fault footwall of the northern Malawi Rift, as recorded by AFT and AHe ages, was interpreted to reflect the linkage of two initially isolated fault segments [*Mortimer et al*., 2016].

In contrast to the Beto Basin, the Galana half-graben trends ~N-S and is bound by a ~90 km, curvilinear fault system comprised of a series of long, contiguous fault segments (Figure 2). Along-strike cooling history trends of the Galana western margin similarly contrast those of the Beto Basin, exhibiting a concurrent early Miocene (~20-18 Ma) onset of observed cooling in the upper 1st and 2nd traverses, which suggests that this portion of the basin-bounding normal fault attained its full length prior to accumulating significant displacement (Figure 7). Such an along-strike, footwall thermal history trend is instead more consistent with the expected denudation pattern for a fault array which developed via an alternative displacement-length evolution, the constant length model [*Walsh et al.*, 2002], in which faults attain their full length relatively early in their development, after which growth is facilitated via displacement accumulation with little elongation [*Morewood and Roberts*, 1999]. A similar concomitant onset of cooling observed in AHe data along-strike of the Jackson and

Pine Forest Ranges of the northwest United States was used by *Curry et al*. [2016] to propose that the fault systems bounding those ranges also developed via this mechanism. Extrapolating a concurrent onset of footwall uplift and denudation to the entire Galana fault system, however, is precluded, due to a lack of thermochronology data from southern and northernmost portions of the fault array.

8 Tectonic Implications

8.1 Potential causes of longitudinal differences in structural evolution of the Broadly Rifted Zone (BRZ)

Significant differences in basin geometries, fault system architecture and basin margin cooling histories indicate that the Beto and Galana basins experienced markedly different structural evolutions. Such contrasting structural evolutions suggests that longitudinal differences in kinematic, mechanical and/or thermal parameters may have existed within the BRZ during its Neogene-Recent rifting history. While it is unclear if the kinematic boundary conditions have remained constant during the Miocene-Recent evolution of the Ethiopian Rift [e.g. *Royer et al.*, 2006; *Corti*, 2009; *DeMets and Merkouriev*, 2016], any such changes should have affected the relatively proximal Beto and Galana Basins equally during their coeval evolutions. Their contrasting fault geometries are not easily explained by differences in mechanical stratigraphy [*Walsh et al.*, 2003; *Schöpfer et al.*, 2006] either, as both master fault systems developed in the Neoproterozoic basement of the Mozambique Belt and overlying Gamo Amaro basalts. Possible west to east differences in the paleo-thermal state of the southern Ethiopian lithosphere are more difficult to determine, in part due to the scarcity of subsurface data in the region. However, indications of major differences in crustal thickness or mantle structure across the modern BRZ which might be suggestive of east-to-west discrepancies in paleo-heat flow are lacking. Instead, estimates of present-day crustal thicknesses across the BRZ are similar [around 30 km; *Keranen and Klemperer*, 2008], albeit poorly constrained. Furthermore, seismic tomography reveals that the broad low-velocity region in the upper mantle beneath Ethiopia extends below the BRZ across its entire width [e.g. *Bastow et al.*, 2008]. Volcanic activity, magmatic emplacement and associated volatile release have also been shown to affect brittle deformation behaviour [e.g. *Ebinger and Casey*, 2001; *Corti et al*., 2003; *Tentler*, 2005; *Rowland et al*., 2007; *Maccaferri et al*., 2014; *Muirhead et al*., 2016]. While the Miocene emplacement of Getra-Kele Basalts in the Chamo and Segen Basins, absent in the Gofa Province [*Ebinger et al*., 2000], suggests that some longitudinal differences in Neogene magmatism across the BRZ exist, neither significant Miocene-Recent volcanism nor the presence of dykes or other intrusives are documented in the immediate Galana basin area [*Woldegabriel et al.*, 1991; *Ebinger et al.*, 1993, 2000; *Philippon et al*., 2014].

One potential parameter that may have led to the contrasting structural evolutionary styles exhibited by the Beto and Galana Basins is the asymmetric distribution of pre-existing basement weaknesses in the BRZ. While much of southern Ethiopia is largely obscured by aerially extensive Cenozoic volcanic cover, widespread Neogene faulting and associated

footwall uplift in the region have provided basement exposure along some basin margins. Moore and Davidson [1978] noted that in the Gofa Province (i.e. Beto Basin), the arcuate pattern of basins and ranges reflect local foliation trends [~N65°E and ~N155°E; *Philippon et al.*, 2014] in the basement gneisses, with faults tending to develop parallel or orthogonal to the basement structures. The markedly similar orientation of the Beto Basin-bounding faults along its northwest (~N45°E) and southwest (~N150°E) margins may suggest that its rift-related structural evolution was influenced by pre-existing, discrete basement fabrics. A similar relationship between fault development and inherited basement heterogeneities has also been proposed for the Chew Bahir Basin, ~50 km to the south [*Philippon et al.*, 2014].

By contrast, crustal fabrics in the eastern BRZ, both discrete and pervasive, trend ~N-S [*Ebinger et al*.,1993; *Keranen and Klemperer*, 2008]. While major faults in the Amaro region parallel local ~N-S basement foliations in the Mozambique Belt, they often cross-cut shallow-dipping mylonites [*Ebinger et al*., 1993], arguing against reactivation of these discrete metamorphic fabrics. Instead, we suggest that the structural evolution of the Galana Basin and easternmost BRZ was influenced by the presence of a deep-seated, Neoproterozoic N-NNE trending suture beneath the region [*Berhe*, 1990; *Stern et al.*, 1990; *Keranen and Klemperer*, 2008], detected by a significant jump in crustal thickness from east (38-40 km) to west (34-36 km) [*Keranen and Klemperer*, 2008]. Penetrative fabrics, such as steep basement shear zones and sutures within mobile belts, provide a matrix of mechanical anisotropies prone to reactivation during extension normal to foliation planes [*Vauchez et al.*, 1997, 1998], which may guide principal stress during rifting [*Daly et al.*, 1989; *Smith and Mosley*, 1993]. The importance of such deep-seated lithospheric anisotropies for the structural evolution of rift segments has been documented throughout the EARS [*Dixon et al.*, 1987; *Versfelt and Rosendahl*, 1989; *Smith and Mosley*, 1993; *Hetzel and Strecker*, 1994; *Morley*, 1999c; *Stuart et al.*, 2006; *Kinabo et al.*, 2007; *Keranen and Klemperer*, 2008; *Keranen et al.*, 2009]. Intriguingly, such an interpretation may also explain the concurrent onset of rift-related cooling in 1st and 2nd traverse samples from the Galana Basin margin. Studies of fault systems elsewhere which developed via re-activation of pre-existing basement structures similarly report fault evolutions involving initial rapid elongation, prior to the accumulation of substantial displacement [e.g. *Walsh et al.*, 2002; *Vétel et al.*, 2005; *Giba et al.*, 2012]. The pervasiveness of steep basement shear zones and sutures throughout the East African Proterozoic mobile belts may explain why an overwhelming majority of crustal-scale normal faults in the EARS are thought to have evolved via the constant length model [e.g. *Morley*, 1999b, 2002].

8.2 EARS evolution and the importance of rheological heterogeneities

The EARS records a complex and spatially disparate late Paleogene-Recent evolution, with associated magmatism and extensional deformation initiating diachronously along its length [*Zeyen et al.*, 1997; *Morley*, 2002; *Morley*, 2010; *Torres Acosta et al.*, 2015]. Its irregular propagation of rifting is thought to have been controlled by rheological heterogeneities and crustal structures inherited from earlier periods of Proterozoic orogenesis and Phanerozoic

rifting [e.g. *Morley et al.*, 1992; *Hetzel and Strecker*, 1994; *Vétel et al.*, 2005; *Bastow et al.*, 2008; *Keranen and Klemperer*, 2008].

In general, volcanism preceded extensional basin formation during the development of the EARS [e.g. *Morley*, 1994; *Morley et al.*, 1999c; *Corti*, 2009]. The earliest known manifestation of EARS-related volcanism occurred in the BRZ and northernmost Turkana Depression ca. 45-35 Ma [*Davidson and Rex*, 1980; *Ebinger et al.*, 1993; *George et al.*, 1998], ~15 Myr before voluminous eruptions in the Afar ca. 31-29 Ma [*Baker et al.*, 1996; *Hofmann et al.*, 1997; *George et al.*, 1998] and Turkana Depression ca. 30 Ma [*Morley et al.*, 1992]. By the Oligocene, EARS-related extension had begun with the development of the ~N-S trending Lokichar and Lothidok basins in the Turkana Depression [*Morley et al.*, 1999b; *Boone et al.*, 2018b]. Both the early onset of volcanism and rift basin formation in the Turkana Depression were likely associated with the region's pre-attenuated lithosphere, thermo-mechanically modified during earlier Cretaceous-early Paleogene Anza-South Sudan rifting and/or Eocene plume impingement [e.g. Morley et al., 1999b; *Ebinger et al.*, 2000]. Consequently, the pre-deformed Turkana lithosphere was perhaps innately weaker [*Morley et al.*, 1992] and/or its shallower lithosphere-asthenosphere boundary allowed for ponding of plume material during the Paleogene [*Ebinger and Sleep*, 1998].

The general lack of Paleogene aged sedimentary rocks, parallelism between Paleogene and Miocene lava flows and the relative consistency in thicknesses of volcanic flows in the BRZ argue against extensional basin development in southern Ethiopia prior to ~20 Ma [*Ebinger et al.*, 2000]. Combined AFT and AHe thermochronology presented in this study suggest an approximately coeval onset of rift-related denudation in the Beto Basin margin and the Amaro Horst during early Miocene time (between ~20-17 Ma), earlier than the middle-late Miocene (14-10 Ma Beto Basin, 10-8 Ma Amaro Horst) initiation suggested by earlier thermal history modelling of AFT data alone [*Balestrieri et al*., 2016] (Section 6.3). Eruptive centres for trachybasalts and tephrites [18.8-12.7 Ma; *Ebinger et al*., 2000] that overlie the Gamo Amaro basalts have been identified along normal faults bounding the Gamo-Gidole Horst along the western Chamo Basin margin, suggesting those faults too had formed prior to ~18 Ma. While a similar early Miocene age has been suggested for the Chew Bahir Basin in the southern BRZ [*Pik et al.*, 2008], other evidence for early Miocene rift basin development elsewhere in the region has been sparse. Instead, widespread extensional basin development in the BRZ was thought to have begun later in the middle-late Miocene [*Corti*, 2009]. However, the refined tectono-thermal evolutions of the Beto and Galana Basin margins presented herein suggest that early Miocene rift basin development in the BRZ may have been more widespread than previously thought, perhaps representing a northward migration of Turkana-related extension into the region [*Bonini et al.*, 2005].

Rift basin formation in the northern MER [~11 Ma; *Wolfenden et al.*, 2004] and central MER [~5-6 Ma; *Bonini et al.*, 2005] began in the late Miocene. Perhaps surprisingly, the MER developed on the eastern edge of the wide (~500 km) mantle upwelling beneath Ethiopia, not above its centre [*Bastow et al.*, 2008]. Instead, the location and initial evolution of the MER is thought to have been controlled by N-NNE trending, lithospheric-scale heterogeneities

associated with the Neoproterozoic suture between East and West Gondwana [*Bastow et al.*, 2008; *Keranen and Klemperer*, 2008; *Keranen et al.*, 2009], which we similarly suggest governed the development of the Galana Basin.

During Miocene-Recent times, extensional basin formation and magmatism within the Turkana region of northern Kenya propagated eastward [*Morley et al.*, 1992, 1999b; *Wescott et al.*, 1999], possibly due to strain hardening of the lithosphere during extension [*Kusznir and Park*, 1987] caused by relatively slow strain rates [between 10^{-16} s^{-1} and 10^{-15} s^{-1}; *Morley*, 1994]. However, the general eastward decrease in age of deformation that is so apparent in central Turkana becomes less clear further north, where all northern Turkana basins may host late Paleogene-Miocene to Pliocene deposits [Figure 26 in *Morley et al.*, 1999b]. Similarly, thermochronology data (this study) and hydrography and geomorphological data [*Woldegabriel and Aronson*, 1987; *Philippon et al.*, 2014] suggest extensional deformation has continued to affect the breadth of the BRZ from Miocene to Recent time.

In the late Pliocene-Pleistocene, faulting and magmatism in the MER and Kenyan Rift localized within narrow zones of minor fault swarms, fissures and eruptive centres [*Ebinger and Casey*, 2001; *Vétel et al.*, 2005; *Vétel and Le Gall*, 2006; *Corti*, 2009]. The fundamental change in structural style from fault-bounded grabens to minor fault swarms may have been governed by the presence of pre-existing lithospheric weakness zones [e.g. *Agostini et al*., 2009; *Corti et al*., 2010, 2013], whereby significant crustal thinning was first accommodated along border faults localized at the margins of the weak zones, followed by the development of internal faults within the graben axis and the upwelling and shallow emplacement of magma beneath the fault swarms [*Hayward and Ebinger*, 1996; *Ebinger*, 2005; *Corti*, 2009]. Narrow zones of fault swarms, intrusions and eruptive centres are, by contrast, absent in the BRZ [*Corti*, 2009]. Yet, the step-fault arrangement of the western Galana Basin margin and the basin-ward migration of rapid rift-related cooling observed in Amaro Horst 1st traverse samples around 13 Ma suggest that some degree of strain migration towards a narrow, interior trough also occurred in the eastern BRZ, relatively early in its development. This basin-wards migration of strain is not observed further west in the Gofa province.

While modern-day extension in the MER, eastern Turkana Depression and Kenyan Rift is accommodated across a narrow (< 100 km) corridor, strain in the BRZ is still distributed across much of its ~ 300 km breadth. Extension in the Gofa Province has largely ceased apart from in its southern sector (e.g. the Beto Basin) where seismicity, hydrography data and master fault scarp morphology, characterized by prominent triangular facets, indicate a degree of ongoing fault activity [*Woldegabriel and Aronson*, 1987; *Philippon et al.*, 2014]. Late Pleistocene-Holocene radiocarbon ages [~26-23 kyr and 7 kyr ; *Philippon et al.*, 2014] from fault gouge collected along the western Galana Basin margin suggest that activity along these structures is also ongoing. As lithospheric strength is fundamentally controlled by crustal thickness [*Kusznir and Park.*, 1987], the unique style of modern deformation in the BRZ may be explained by its distinct rheological characteristics resulting from the northward thickening of the crust from the Turkana Depression [~20 km, *Benoit et al.*, 2006a] to the BRZ [~30 km; *Keranen and Klemperer*, 2008]. *Kusznir and Park* [1987] showed that above a

critical lithospheric extension factor (β) of 1.5, slow strain rates lead to rapid strain hardening. Therefore, the reduced degree of crustal thinning experienced by the BRZ [maximum β of 1.2, *Ebinger et al.*, 1989] compared to that of Turkana [maximum β of 1.55-1.65, *Hendrie et al.*, 1994] may have thus far prevented the onset of significant strain hardening. Nevertheless, the hot, thin lithosphere of the BRZ still promotes widely-distributed deformation.

9 Conclusions

Low-temperature thermochronology data constrain the timing of Beto and Galana Basin formation to be early Miocene in age (~20-17 Ma). These findings, along with previously published AHe data interpreted as indicating a concurrent (~20 Ma) formation of the Chew Bahir Basin, suggest that EARS-related extension began concurrently across the width of the BRZ in the early Miocene, at least 7 Myr prior to the formation of the late Miocene MER further north. The earlier initiation of rifting in the BRZ may be related to either the inherent weakness of the regional lithosphere, thermo-mechanically modified by earlier Cretaceous-early Paleogene Anza-South Sudan rifting, Eocene plume impingement, or some combination of the two. Earlier lithospheric modification in the region may also be responsible for Neogene EARS extension being accommodated by a diffuse zone of deformation, as opposed to the MER's narrow rift morphology that developed above the thicker crust of central Ethiopia.

Combined AFT and AHe thermochronology presented herein reveal spatially and temporally variable basin margin denudation patterns that appear to reflect the disparate structural architecture of their respective basin-bounding fault arrays. Along strike differences in thermal history models are consistent with the normal fault array bounding the Beto Basin initially developing as isolated and kinematically independent fault segments, which linked relatively late in their history after already accumulating significant displacement. By contrast, low-temperature thermochronology data suggest that the northern portion of the Galana Basin-bounding fault system had approached at least a considerable portion of its final length prior to the accumulation of significant displacement. A lack of low-temperature thermochronology data from the southern Galana margin preclude an assessment of its thermal history. At ~13 Ma, strain in the Galana Basin began to migrate towards the graben axis, forming a new normal fault, or faults, in the former hanging wall. This marked the beginning of a pattern of strain localisation and progressive narrowing of the zone of deformation in the eastern BRZ, not exhibited further west in the Gofa province. However, unlike in the MER and northern Kenyan Rift, where large boundary faults were abandoned in favour of low-displacement fault swarms and associated intrusive complexes, border faults across the BRZ remain active.

While acknowledging the potential importance of magma-fault interaction during the development of volcanic rifts, the lack of significant Miocene-Recent magmatism in the regions of interest argues against such an influence on the structural evolution of the Beto and Galana Basins. Instead, we suggest that the longitudinal contrast in boundary fault system

growth primarily reflects differences in the distribution of pre-existing lithospheric heterogeneities in the BRZ. The highly-segmented fault system bounding the Beto Basin reflects local basement foliation trends in the west of the region, while the long, linear faults defining the Galana western margin mirror a N-NNE trending, Neoproterozoic suture zone beneath the eastern BRZ.

Acknowledgements

We note that there are no data sharing issues. All numerical information is provided in the tables. Funding for this research was provided through Australian Research Council grant DP130101610. SCB received additional support from the MIFRS and MIRS scholarships and the Baragwanath Geology Research Scholarship awarded by the University of Melbourne. The University of Melbourne Thermochronology Lab receives infrastructure support under the AuScope program of NCRIS. Technical assistance provided by Abaz Alimanovic for (U-Th)/He analyses are greatly appreciated. The article benefited from the suggestions provided by Peter van der Beek and Manfred Strecker and constructive reviews from John Geissman and Christopher Morley.

Figure Captions

Figure 1. Overview maps of the study area. a: Topographic map of Africa showing the location of the East African Rift System (EARS). b: Topographic map of the Broadly Rifted Zone (BRZ) and Turkana Depression, illustrating their spatial relationship with the narrow Main Ethiopian Rift (MER) and Kenyan Rift, and the transverse Cretaceous-early Paleogene Anza Rift (grey). c: Simplified geological map of the BRZ with the Beto Basin in the west and Amaro Horst in the east. Red boxes depict the study areas, corresponding to Figures 2a and 2b. LAR = Lapur Range; LO = Lokichar Basin; NLO = North Lokichar Basin. Geological map after Davidson [1983], Mengesha et al. [1996], Ebinger et al. [2000], Philippon et al. [2014] and Balestrieri et al. [2016].

Figure 2. Geological maps of the Beto Basin (a) and Amaro Horst (b) regions with sample localities. The AFT age [Ma ± 1σ] and mean track length (MTL) [μm ± 1 s.d.] data [*Balestrieri et al*., 2016] for samples AM1-West and AM1-South are shown. Remaining AFT data from this and previous studies are shown in Figure 3. Geological maps after *Balestrieri et al*. [2016], *Davidson* [1983], *Ebinger et al.* [1993], *Levitte et al*. [1974] and *Woldegabriel et al*. [1997]. Stereoplots with rose diagrams of faults in the Gofa Province and Amaro Horst region, and obtained directions of extension adapted from *Ebinger et al*. [1993] and *Philippon et al*. [2014].

Figure 3. Pseudo 3-D geological cross-sections of Beto and Galana Basins, orthogonal to basin-bounding normal faults, and sample localities. Previously published AFT ages [Ma ± 1σ] and mean track lengths (MTL) [μm ± 1 s.d.] [*Philippon et al.*, 2014; *Balestrieri et al*., 2016] are shown in boxes with grey backgrounds. Augmented MTL data presented in this study are shown with white backgrounds. A ~NW-SE transect of the SW Beto Basin margin

is also shown (location illustrated in Figure 2). Fault planes discussed in text are schematically illustrated in grey. Note, the western fault illustrated in the Amaro Horst 3D cross-section does not extend through to the 2nd traverse. Fault geometries are based on surface observations [*Levitte et al*., 1974; *Ebinger et al*., 1993; *Woldegabriel et al*., 1997] and are not constrained at depth. Fault dips appear steeper due to vertical exaggeration of cross-sections.

Figure 4. Plots of AHe age versus eU content (left column), versus equivalent spherical radius (middle column) and versus apatite crystal morphology (right column). In general, AHe ages do not exhibit strong correlations with grain size, morphology or eU content. Possible exceptions are discussed in Section 4.2.

Figure 5. Boomerang plots of AFT age versus MTL (circles) for Beto Basin and Amaro Horst basement rock samples. Single grain AHe ages are displayed as stars, with 2T grains outlined in black. Note, three Beto Basin NW margin AHe single grain ages from sample GR13 (40.2 ± 2.5 Ma, 40.3 ± 2.5 Ma, and 89.7 ± 5.6 Ma) are not shown. Approximate duration of tectono-thermal events recorded by AFT and AHe data are marked by grey bars. Dark grey arrows represent inferred boomerang curves. See Section 5 for description of a boomerang plot and data interpretation.

Figure 6. Thermal history models of Beto Basin and Amaro Horst samples generated using the *QTQt* software, following the protocol described in Section 6. Where possible, samples were grouped together as vertical transects during thermal history modelling (i.e. Beto Basin SW margin samples and Amaro Horst upper 1st traverse, lower 1st traverse and 2nd traverse samples). The posterior probability distribution of accepted time-temperature paths is represented by the colour map, with warmer colours indicating higher probabilities. Black hashed lines represent the best fit time-temperature path, while solid black lines represent the 95% confidence interval limits. A plot of observed versus predicted AFT and AHe ages accompanies each thermal history model. AHe ages are displayed with resampling errors (see text). Single sample thermal history models are also accompanied by a plot of observed confined track distribution overlain by the predicted distribution (red curve) and the 95% confidence interval (grey curves) of the predicted distribution. Plots of observed and predicted confined track distributions for vertical transect thermal history models are presented in the Supporting Information (Figure S3).

Figure 7. Fault displacement (D)-length (L) relationships and along-strike, footwall cooling history trends for end-member, normal fault array growth models (**a, b**) and the Beto Basin- (**c**) and Galana Basin-bounding fault systems (**d**). **a)** Segment growth and linkage model, where multiple (in this case two), initially independent fault segments grow via tip propagation, before interacting and linking to form a through-going fault array [*Anders and Schlische*, 1994; *Cartwright et al*., 1995; *Gawthorpe and Leeder*, 2000; *Gupta et al*., 1998; *Peacock and Sanderson*, 1994; *Trudgill and Cartwright*, 1994]. Prior to linking, the adjacent fault segments begin to mechanically interact, often producing asymmetric D-L profiles (t2) [e.g. Peacock and Sanderson, 1994; Cartwright et al., 1995; Gawthorpe and

Leeder, 2000]. After linkage, the segment coinciding with the area of paleo-fault linkage (green circle) is initially under-displaced (t3). It must therefore, rapidly accumulate displacement in order for the linked fault array to develop an appropriate D/L profile (t4) [Gawthorpe and Leeder, 2000]. b) Constant length model, in which a fault system approaches or obtains its full length, perhaps by the linkage of smaller faults, but prior to the accumulation of significant displacement [*Morewood and Roberts*, 1999; *Morley*, 1999b; *Walsh et al.*, 2002, 2003]. For each fault growth model, theoretical cooling histories are presented for three basement rock samples (red, green and blue circles) from the base of the fault scarp. Relative cooling magnitudes for each rock sample are shown for time periods 0-4, corresponding to the four stages of fault growth illustrated in the D/L plot, whereby cooling is assumed to be inversely proportional to displacement. Time 0 represents the period prior to fault array formation. D/L plots adapted from *Kim and Sanderson* [2005]. **c, d)** The Beto and Amaro Horst (Galana Basin), where along-strike, footwall cooling histories are determined by thermal history modelling results (best-fit time-temperature paths; Fig. 6). Assuming fault displacement is proportional to footwall cooling, along-strike differences in cooling history are used to estimate possible D/L curves at different stages of basin-bounding fault array growth (dashed lines). Note, the thermal evolution of the southern Amaro Horst is not constrained due to a lack of data.

References

Anders, M. H., and R. W. Schlische (1994), Overlapping Faults, Intrabasin Highs, and the Growth of Normal Faults, *J. Geol.*, *102*, 165–180.

Arambourg, C., and R. G. Wolff (1969), Nouvelles données paléontologique sur l'âge des "Gres du Lubur" (Turkana Grits) al'ouest du lac Rodolphe, *Comptes Rendus Société géologique Fr.*, *9*, 190–202.

Baker, B. H., P. A. Mohr, and L. A. J. Williams (1972), Geology of the Eastern Rift System of Africa, in *Geological Society of America Special Papers*, vol. 136, pp. 1–68.

Baker, J., L. Snee, and M. Menzies (1996), A brief Oligocene period of flood volcanism in Yemen: implications for the duration and rate of continental flood volcanism at the Afro-Arabian triple junction, *Earth Planet. Sci. Lett.*, *138*, 39–55.

Balestrieri, M. L., F. M. Stuart, C. Persano, E. Abbate, and G. Bigazzi (2005), Geomorphic development of the escarpment of the Eritrean margin, southern Red Sea from combined apatite fission-track and (U–Th)/He thermochronometry, *Earth Planet. Sci. Lett.*, *231*, 97–110, doi:10.1029/2001JB001009.

Balestrieri, M. L., M. Bonini, G. Corti, F. Sani, and M. Philippon (2016), A refinement of the chronology of rift-related faulting in the Broadly Rifted Zone, southern Ethiopia, through apatite fission-track analysis, *Tectonophysics*, *671*, 42–55, doi:10.1016/j.tecto.2016.01.012.

Barbarand, J., A. Carter, I. Wood, and T. Hurford (2003), Compositional and structural control of fission-track annealing in apatite, *Chem. Geol.*, *198*(1–2), 107–137, doi:10.1016/S0009-2541(02)00424-2.

Barnett, J. A., J. Mortimer, J. H. Rippon, J. J. Walsh, and J. Watterson (1987), Displacement geometry in the volume containing a single normal fault, *Am. Assoc. Pet. Geol. Bull.*,

71(8), 925–937.

Bastow, I. D., G. W. Stuart, J.-M. Kendall, and C. J. Ebinger (2005), Upper-mantle seismic structure in a region of incipient continental breakup: northern Ethiopian rift, *Geophys. J. Int.*, *162*, 479–493, doi:10.1111/j.1365-246X.2005.02666.x.

Bastow, I. D., A. A. Nyblade, G. W. Stuart, T. O. Rooney, and M. H. Benoit (2008), Upper mantle seismic structure beneath the Ethiopian hot spot: Rifting at the edge of the African low-velocity anomaly, *Geochemistry, Geophys. Geosystems*, *9*(12), doi:10.1029/2008GC002107.

Bastow, I. D., D. Keir, and E. Daly (2011), The Ethiopia Afar Geoscientific Lithospheric Experiment (EAGLE): Probing the transition from continental rifting to incipient seafloor spreading, *Geol. Soc. Am. Spec. Pap.*, *478*, doi:10.1130/2011.2478(04).

Bendick, R., S. McClusky, R. Bilham, L. Asfaw, and S. Klemperer (2006), Distributed Nubia–Somalia relative motion and dike intrusion in the Main Ethiopian Rift, *Geophys. J. Int.*, *165*, 303–310, doi:10.1111/j.1365-246X.2006.02904.x.

Benoit, M. H., A. A. Nyblade, and M. E. Pasyanos (2006), Crustal thinning between the Ethiopian and East African plateaus from modeling Rayleigh wave dispersion, *Geophys. Res. Lett.*, doi:10.1029/2006GL025687.

Berhe, S. M. (1990), Ophiolites in Northeast and East Africa: implications for Proterozoic crustal growth, *J. Geol. Soc. London*, *147*, 41–57.

Boccaletti, M., M. Bonini, R. Mazzuoli, B. Abebe, L. Piccardi, and L. Tortorici (1998), Quatemary oblique extensional tectonics in the Ethiopian Rift (Horn of Africa), *Tectonophysics*, *287*, 97–116.

Bonini, M., T. Souriot, M. Boccaletti, and J. P. Brun (1997), Succesive orthogonal and oblique extension episodes in a rift zone: Laboratory experiments with application to the Ethiopian Rift, *Tectonics*, *16*(2), 347–362.

Bonini, M., G. Corti, F. Innocenti, P. Manetti, F. Mazzarini, T. Abebe, and Z. Pecskay (2005), Evolution of the Main Ethiopian Rift in the frame of Afar and Kenya rifts propagation, *Tectonics*, *24*(1), n/a-n/a, doi:10.1029/2004TC001680.

Boone, S. C., C. Seiler, A. J. Reid, B. Kohn, and A. Gleadow (2016), An Upper Cretaceous paleo-aquifer system in the Eromanga Basin of the central Gawler Craton, South Australia: evidence from apatite fission track thermochronology, *Aust. J. Earth Sci.*, *63*(3), 315–331, doi:10.1080/08120099.2016.1199050.

Boone, S. C., C. Seiler, B. P. Kohn, A. J. W. Gleadow, D. A. Foster, and L. Chung (2018a), Influence of Rift Superposition on Lithospheric Response to East African Rift System Extension: Lapur Range, Turkana, Kenya, *Tectonics*, *37*, 1–26, doi:10.1002/2017TC004575.

Boone, S. C., B. P. Kohn, A. J. W. Gleadow, C. K. Morley, C. Seiler, D. A. Foster, and L. Chung (2018b), Tectono-thermal evolution of a long-lived segment of the East African Rift System: Thermochronological insights from the North Lokichar Basin, Turkana, Kenya, *Tectonophysics*, *744*, 23-46, doi:10.1016/j.tecto.2018.06.010.

Bosworth, W., M. R. Strecker, and P. M. Blisniuk (1992), Integration of East African Paleostress and Present-Day Stress Data: Implications for Continental Stress Field Dynamics, *J. Geophys. Res.*, *97*(B8), 11,851-11,865, doi:10.1029/90JB02568.

Brown, R. W., R. Beucher, S. Roper, C. Persano, F. Stuart, and P. Fitzgerald (2013), Natural

age dispersion arising from the analysis of broken crystals. Part I: Theoretical basis and implications for the apatite (U-Th)/He thermochronometer, *Geochim. Cosmochim. Acta*, *122*(120), 478–497, doi:10.1016/j.gca.2013.05.041.

Brown, S. J., J. R. Thigpen, J. A. Spotila, W. C. Krugh, L. M. Tranel, and D. A. Orme (2017), Onset Timing and Slip History of the Teton Fault, Wyoming: A Multidisciplinary Reevaluation, *Tectonics*, *36*, doi:10.1002/2016TC004462.

Bürgmann, R., D. D. Pollard, and S. J. Martel (1994), Slip distribution on faults: effects of stress gradients, inelastic deformation, heterogeneous host-rock stiffness, and fault interaction, *J. Struct. Geol.*, *16*(12), 1675–1690.

Cartwright, J. A., B. D. Trudgill, and C. S. Mansfield (1995), Fault growth by segment linkage: an explanation for scatter in maximum displacement and trace length data from the Canyonlands Grabens of SE Utah, *J. Struct. Geol.*, *17*(9), 1319–1326.

Childs, C., T. Manzocchi, J. J. Walsh, C. G. Bonson, A. Nicol, and M. P. J. Schöpfer (2009), A geometric model of fault zone and fault rock thickness variations, *J. Struct. Geol.*, *31*, 117–127, doi:10.1016/j.jsg.2008.08.009.

Chorowicz, J. (2005), The East African rift system, *J. African Earth Sci.*, *43*(1), 379–410, doi:10.1016/j.jafrearsci.2005.07.019.

Commins, D., S. Gupta, and J. Cartwright (2005), Deformed streams reveal growth and linkage of a normal fault array in the Canyonlands graben, Utah, *Geology*, *33*(8), 645–648, doi:10.1130/G21433.1.

Corti, G. (2009), Continental rift evolution: From rift initiation to incipient break-up in the Main Ethiopian Rift, East Africa, *Earth-Science Rev.*, *96*(1–2), 1–53, doi:10.1016/j.earscirev.2009.06.005.

Corti, G., M. Bonini, S. Conticelli, F. Innocenti, P. Manetti, and D. Sokoutis (2003), Analog modelling of continental extension: a review focused on the relations between the patterns of deformation and the presence of magma, Earth-Science Rev., 63(3–4), 169–247, doi:10.1016/S0012-8252(03)00035-7.

Corti, G., I. Iandelli, and M. Cerca (2010), Experimental modeling of rifting at craton margins, *Geosphere*, *9*, 138–154.

Corti, G., G. Ranalli, A. Agostini, and D. Sokoutis (2013), Inward migration of faulting during continental rifting: Effects of pre-existing lithospheric structure and extension rate, *Tectonophysics*, *594*, 137–148.

Cowie, P. A., and Z. O. E. K. Shipton (1998), Fault tip displacement gradients and process zone dimensions, *J. Struct. Geol.*, *20*(8), 983–997.

Curry, M. A. E., J. B. Barnes, and J. P. Colgan (2016), Testing fault growth models with low-temperature thermochronology in the northwest Basin and Range, USA, *Tectonics*, *35*, 2467–2492, doi:10.1002/2016TC004211.Received.

Daly, M. C., J. Chorowicz, and J. D. Fairhead (1989), Rift basin evolution in Africa: The influence of reactivated steep basement shear zones, *Geol. Soc. Spec. Publ.*, *44*, 309–334, doi:10.1144/GSL.SP.1989.044.01.17.

Danišik, M., R. F. Sachsenhofer, V. A. Privalov, E. A. Panova, W. Frisch, and C. Spiegel (2008), Low-temperature thermal evolution of the Azov Massif (Ukrainian Shield–Ukraine) — Implications for interpreting (U–Th)/He and fission track ages from cratons, *Tectonophysics*, *456*, 171–179, doi:10.1016/j.tecto.2008.04.022.

Davidson, A. (1983), *The Omo River Project: reconnaissance geology and geochemistry of parts of Ilubabor, Kefa, Gemu Gofa and Sidamo, Ethiopia*.

Davidson, A., and D. C. Rex (1980), Age of volcanism and rifting in southwestern Ethiopa, *Nature*, *283*, 657–658.

Davies, S. J., N. H. Dawers, A. McLeod, and J. R. Underhill (2000), The structural and sedimentological evolution of early synrift successions: the Middle Jurassic Tarbert Formation, North Sea, *Basin Res.*, *12*, 343–365.

Dawers, N. H., and J. R. Underhill (2000), The role of fault interaction and linkage in controlling synrift stratigraphic sequences: Late Jurassic, Stratfjord East Area, northern North Sea, *Am. Assoc. Pet. Geol. Bull.*, *84*(1), 45–64.

DeMets, C., and S. Merkouriev (2016), High-resolution estimates of Nubia–Somalia plate motion since 20 Ma from reconstructions of the Southwest Indian Ridge, Red Sea and Gulf of Aden, *Geophysical Journal International, 207*, 317-332.

Densmore, A. L., and R. Guidon (2005), What sets topographic relief in extensional footwalls?, *Geology*, *33*(6), 453–456, doi:10.1130/G21440.1.

Densmore, A. L., N. H. Dawers, S. Gupta, R. Guidon, and T. Goldin (2004), Footwall topographic development during continental extension, *J. Geophys. Res.*, *109*, 1–16, doi:10.1029/2003JF000115.

Densmore, A. L., S. Gupta, P. A. Allen, and N. H. Dawers (2007), Transient landscapes at fault tips, *J. Geophys. Res.*, *112*, 1–16, doi:10.1029/2006JF000560.

Densmore, A. L., R. Hetzel, S. Ivy-ochs, W. C. Krugh, N. Dawers, P. Kubik, and R. Range (2009), Spatial variations in catchment-averaged denudation rates from normal fault footwalls, *Geology*, *37*(12), 1139–1142, doi:10.1130/G30164A.1.

Dixon, T. H., R. J. Stern, and I. M. Hussein (1987), Control of Red Sea Rift Geometry by Precambrian Structures, *Tectonics*, *6*(5), 551–571, doi:10.1029/TC006i005p00551.

Ebinger, C. (2005), Continental break-up: The East African perspective, *Astron. Geophys.*, *46*(2), 2–16.

Ebinger, C., T. D. Bechtel, D. W. Forsyth, and C. O. Bowin (1989), Effective elastic plate thickness beneath the East African and Afar domes, *J. Geophys. Res.*, *94*(B3), 2883–2901.

Ebinger, C. J., and M. Casey (2001), Continental breakup in magmatic provinces: An Ethiopian example, *Geology*, *29*(6), 527–530.

Ebinger, C. J., and N. H. Sleep (1998), Cenozoic magnatism throughout east Africa resulting from impact of a single plume, *Nature*, *395*, 788–791.

Ebinger, C. J., T. Yemane, G. Woldegabriel, J. L. Aronson, and R. C. Walter (1993), Late Eocene-Recent volcanism and faulting in the southern main Ethiopian rift, *J. Geol. Soc. London.*, *150*(1), 99–108, doi:10.1144/gsjgs.150.1.0099.

Ebinger, C. J., T. Yemane, D. J. Harding, S. Tesfaye, S. Kelley, and D. C. Rex (2000), Rift deflection, migration, and propagation: Linkage of the Ethiopian and Eastern rifts, Africa, *GSA Bull.*, *112*(2), 163–176.

Ehlers, T. A. (2005), Crustal Thermal Processes and the Interpretation of Thermochronometer Data, *Rev. Mineral. Geochemistry*, *58*(August), 315–350, doi:10.2138/rmg.2005.58.12.

Farley, K. A. (2000), Helium diffusion from apatite: General behavior as illustrated by

Durango fluorapatite, *J. Geophys. Res.*, *105*(B2), 2903–2914.
Farley, K. A., and D. F. Stockli (2002), (U-Th)/ He Dating of Phosphates: Apatite, Monazite, and Xenotime, *Rev. Mineral. Geochemistry*, *48*(1), 559–577, doi:10.2138/rmg.2002.48.15.
Farley, K. A., R. A. Wolf, and L. T. Silver (1996), The effects of long alpha-stopping distances on (U-Th)/He ages, *Geochim. Cosmochim. Acta*, *60*(21), 4223–4229, doi:10.1016/S0016-7037(96)00193-7.
Fernandes, R. M. S., B. A. C. Ambrosius, R. Noomen, L. Bastos, L. Combrinck, J. M. Miranda, and W. Spakman (2004), Angular velocities of Nubia and Somalia from continuous GPS data: implications on present-day relative kinematics, *Earth Planet. Sci. Lett.*, *222*, 197–208, doi:10.1016/j.epsl.2004.02.008.
Fishwick, S. (2010), Surface wave tomography: Imaging of the lithosphere–asthenosphere boundary beneath central and southern Africa?, *Lithos*, *120*, 63–73, doi:10.1016/j.lithos.2010.05.011.
Fitzgerald, P. G. (1992), The Transantacrtic Mountains of Southern Victoria Land: The Application of Apatite Fission Track Analysis to a Rift Shoulder Uplift, *Tectonics*, *11*(3), 634–662.
Fitzgerald, P. G., S. L. Baldwin, L. E. Webb, and P. B. O'Sullivan (2006), Interpretation of (U-Th)/He single grain ages from slowly cooled crustal terranes: A case study from the Transantarctic Mountains of southern Victoria Land, *Chem. Geol.*, *225*(1–2), 91–120, doi:10.1016/j.chemgeo.2005.09.001.
Fleischer, R., P. Price, and R. Walker (1975), *Nuclear Tracks in Solids: principles and applications*, University of California Press, Berkeley.
Flowers, R. M., and S. A. Kelley (2011), Interpreting data dispersion and "inverted" dates in apatite (U–Th)/He and fission-track datasets: An example from the US midcontinent, *Geochim. Cosmochim. Acta*, *75*(18), 5169–5186, doi:10.1016/j.gca.2011.06.016.
Flowers, R. M., D. L. Shuster, B. P. Wernicke, and K. A. Farley (2007), Radiation damage control on apatite (U-Th)/He dates from the Grand Canyon region, Colorado Plateau, *Geology*, *35*(5), 447–450, doi:10.1130/G23471A.1.
Flowers, R. M., R. A. Ketcham, D. L. Shuster, and K. A. Farley (2009), Apatite (U-Th)/He thermochronometry using a radiation damage accumulation and annealing model, *Geochim. Cosmochim. Acta*, *73*(8), 2347–2365, doi:10.1016/j.gca.2009.01.015.
Flowers, R. M., K. A. Farley, and R. A. Ketcham (2015), A reporting protocol for thermochronologic modeling illustrated with data from the Grand Canyon, *Earth Planet. Sci. Lett.*, *432*, 425–435, doi:10.1016/j.epsl.2015.09.053.
Fossen, H., and A. Rotevatn (2016), Fault linkage and relay structures in extensional settings — A review, *Earth Sci. Rev.*, *154*, 14–28, doi:10.1016/j.earscirev.2015.11.014.
Foster, A. N., and J. A. Jackson (1998), Source parameters of large African earthquakes: implications for crustal rheology and regional kinematics, *Geophys. J. Int.*, *134*, 422–448.
Foster, D. A., and A. J. W. Gleadow (1992), The morphotectonic evolution of rift-margin mountains in central Kenya: Constraints from apatite fission-track thermochronology, *Earth Planet. Sci. Lett.*, *113*(1–2), 157–171, doi:10.1016/0012-821X(92)90217-J.
Foster, D. A., and A. J. W. Gleadow (1993), Episodic Denudation in East Africa: A Legacy

of Intracontinental Tectonism, *Geophys. Res. Lett.*, *20*(21), 2395–2398.
Foster, D. A., and J. W. Gleadow (1996), Structural framework and denudation history of the flanks of the Kenya and Anza Rifts , East Africa, *Tectonics*, *15*(2), 258–271, doi:10.1029/95TC02744.
Galbraith, R. F. (1981), On statistical models for fission track counts, Journal of the International Association for Mathematical *Geology*, *13*(6), 471–478.
Gallagher, K. (1995), Evolving temperature histories from apatite fission-track data, *Earth Planet. Sci. Lett.*, *136*(3–4), 421–435.
Gallagher, K. (2012), Transdimensional inverse thermal history modeling for quantitative thermochronology, *J. Geophys. Res. Solid Earth*, *117*, doi:10.1029/2011JB008825.
Gallagher, K., C. J. Hawkesworth, and M. S. M. Mantovani (1994), The denudation history of the onshore continental margin of SE Brazil inferred from apatite fission track data, *J. Geophys. Res.*, *99*(B9), 18,117-18,145.
Gallagher, K., and R. Brown (1997), The onshore record of passive margin evolution, *J. Geol. Soc. London*, *154*, 451–457, doi:10.1144/gsjgs.154.3.0451.
Gallagher, K., and R. A. Ketcham (2018), Comment on "Thermal history modelling: HeFTy vs. QTQt" by Vermeesch and Tian, Earth-Science Reviews (2014), 139, 279-290, *Earth-Science Rev.*, *176*, 387–394, doi:10.1016/j.earscirev.2017.11.001.
Gautheron, C., L. Tassan-Got, J. Barbarand, and M. Pagel (2009), Effect of alpha-damage annealing on apatite (U-Th)/He thermochronology, *Chem. Geol.*, *266*, 157–170, doi:10.1016/j.chemgeo.2009.06.001.
Gautheron, C., J. Barbarand, R. A. Ketcham, L. Tassan-Got, P. van der Beek, M. Pagel, R. Pinna-Jamme, F. Couffignal, and M. Fialin (2013), Chemical influence on α-recoil damage annealing in apatite: Implications for (U–Th)/He dating, *Chem. Geol.*, *351*, 257–267, doi:10.1016/j.chemgeo.2013.05.027.
Gawthorpe, R. L., and M. R. Leeder (2000), Tectono-sedimentary evolution of active extensional basins, *Basin Res.*, *12*, 195–218.
Gawthorpe, R. L., I. Sharp, J. R. Underhill, and S. Gupta (1997), Linked sequence stratigraphic and structural evolution of propagating normal faults, *Geology*, *25*(9), 795–798, doi:10.1144/GSL.SP.2000.172.01.09.
Gawthorpe, R. L., C. A. Jackson, M. J. Young, I. R. Sharp, A. R. Moustafa, and C. W. Leppard (2003), Normal fault growth, displacement localisation and the evolution of normal fault populations: the Hammam Faraun fault block, Suez rift, Egypt, *J. Struct. Geol.*, *25*, 883–895.
George, R., N. Rogers, and S. Kelley (1998), Earliest magnatism in Ethiopia: Evidence for two mantle plumes in one flood basalt province, *Geology*, *26*(10), 923–926.
Giba, M., J. J. Walsh, and A. Nicol (2012), Segmentation and growth of an obliquely reactivated normal fault, *J. Struct. Geol.*, *39*, 253–267, doi:10.1016/j.jsg.2012.01.004.
Gleadow, A., M. Harrison, B. Kohn, R. Lugo-zazueta, and D. Phillips (2015), The Fish Canyon Tuff a new low temperature thermochronology standard, *Earth Planet. Sci. Lett.*, *424*, 95–108, doi:10.1016/j.epsl.2015.05.003.
Gleadow, A. J. W., and I. R. Duddy (1981), A Natural Long-Term Track Annealing Experiment for Apatite, *Nucl. Tracks*, *5*(1–2), 169–174.
Green, P. F., I. R. Duddy, A. J. W. Gleadow, and J. F. Lovering (1989), Apatite Fission-

Track Analysis as a Paleotemperature Indicator for Hydrocarbon Exploration, in *Thermal History of Sedimentary Basins, Methods and Case Histories*, edited by N. D. Naeser and T. H. McCulloh, pp. 181–196, Springer-Verlag, New York.

Guenthner, W. R., P. W. Reiners, R. A. Ketcham, L. Nasdala, and G. Giester (2013), Helium diffusion in natural zircon: radiation damage, anisotropy, and the interpretation of zircon (U-TH)/He thermochronology, *Am. J. Sci.*, *313*(3), 145–198, doi:10.2475/03.2013.01.

Gunnell, Y., K. Gallagher, A. Carter, M. Widdowson, and A. J. Hurford (2003), Denudation history of the continental margin of western peninsular India since the early Mesozoic - reconciling apatite fission-track data with geomorphology, *Earth Planet. Sci. Lett.*, *215*, 187–201, doi:10.1016/S0012-821X(03)00380-7.

Gupta, S., P. A. Cowie, N. H. Dawers, and J. R. Underhill (1998), A mechanism to explain rift-basin subsidence and stratigraphic patterns through fault-array evolution, *Geology*, *26*(7), 595–598, doi:10.1130/0091-7613(1998)026<0595.

Harbor, D. J. (1997), Landscape evolution at the margin of the Basin and Range, *Geology*, *25*(12), 1111–1114.

Hayward, N. J., and C. J. Ebinger (1996), Variations in the along-axis segmentation of the Afar Rift system, *Tectonics*, *15*(2), 244–257.

Hendrie, D. B., N. J. Kusznir, C. K. Morley, and C. J. Ebinger (1994), Cenozoic extension in northern Kenya: a quantitative model of rift basin development in the Turkana region, *Tectonophysics*, *236*(1–4), 409–438, doi:10.1016/0040-1951(94)90187-2.

Hetzel, R., and M. R. Strecker (1994), Late Mozambique Belt structures in western Kenya and their influence on the evolution of the Cenozoic Kenya Rift, *J. Struct. Geol.*, *16*(2), 189–201, doi:10.1016/0191-8141(94)90104-X.

Hofmann, C., V. Courtillot, G. Féraud, P. Rochette, G. Yirgu, E. Ketefo, and R. Pik (1997), Timing of the Ethiopian flood basalt event and implications of Plume birth and global change, *Nature*, *389*, 838–841, doi:10.1038/39853.

Jackson, C. A., and A. Rotevatn (2013), 3D seismic analysis of the structure and evolution of a salt-influenced normal fault zone: A test of competing fault growth models, *J. Struct. Geol.*, *54*, 215–234, doi:10.1016/j.jsg.2013.06.012.

Keir, D., C. J. Ebinger, G. W. Stuart, E. Daly, and A. Ayele (2006), Strain accommodation by magmatism and faulting as rifting proceeds to breakup: Seismicity of the northern Ethiopian rift, *J. Geophys. Res.*, *111*, 1–17, doi:10.1029/2005JB003748.

Keranen, K., and S. L. Klemperer (2008), Discontinuous and diachronous evolution of the Main Ethiopian Rift: Implications for development of continental rifts, *Earth Planet. Sci. Lett.*, *265*, 96–111, doi:10.1016/j.epsl.2007.09.038.

Keranen, K. M., S. L. Klemperer, J. Julia, J. F. Lawrence, and A. A. Nyblade (2009), Low lower crustal velocity across Ethiopia: Is the Main Ethiopian Rift a narrow rift in a hot craton?, *Geochemistry, Geophys. Geosystems*, *10*, 1–21, doi:10.1029/2008GC002293.

Ketcham, R. A. (2005), Forward and Inverse Modeling of Low- Temperature Thermochronometry Data, *Rev. Mineral. Geochemistry*, *58*, 275–314, doi:10.2138/rmg.2005.58.11.

Ketcham, R. A., A. Carter, R. A. Donelick, J. Barbarand, and A. J. Hurford (2007a), Improved measurement of fission-track annealing in apatite using c-axis projection, *Am. Mineral.*, *92*(5–6), 789–798, doi:10.2138/am.2007.2280.

Ketcham, R. A., A. Carter, R. A. Donelick, J. Barbarand, and A. J. Hurford (2007b), Improved modeling of fission-track annealing in apatite, *Am. Mineral.*, *92*, 799–810, doi:10.2138/am.2007.2281.

Kim, Y., and D. J. Sanderson (2005), The relationship between displacement and length of faults: a review, *Earth-Science Rev.*, *68*, 317–334, doi:10.1016/j.earscirev.2004.06.003.

Kinabo, B. D., E. A. Atekwana, J. P. Hogan, M. P. Modisi, D. D. Wheaton, and A. B. Kampunzu (2007), Early structural development of the Okavango rift zone, NW Botswana, *J. African Earth Sci.*, *48*, 125–136, doi:10.1016/j.jafrearsci.2007.02.005.

Kohn, B. P., A. J. W. Gleadow, R. W. Brown, K. Gallagher, M. Lorencak, and W. P. Noble (2005), Visualizing Thermotectonic and Denudational Histories Using Apatite Fission Track Thermochronology, *Rev. Mineral. Geochemistry*, *58*, 527–565, doi:10.2138/rmg.2005.58.20.

Kohn, B. P., M. Lorencak, A. J. W. Gleadow, F. Kohlmann, A. Raza, K. G. Osadetz, and P. Sorjonen-ward (2009), A reappraisal of low-temperature thermochronology of the eastern Fennoscandia Shield and radiation-enhanced apatite fission-track annealing, in *Thermochronological Methods: From Palaeotemperature Constraints to Landscape Evolution Models*, edited by F. Lisker, B. Ventura, and U. A. Glasmacher, pp. 193–216, Geological Society of London, London.

Kusznir, N. J., and R. G. Park (1987), The extensional strength of the continental lithosphere: its dependence on geothermal gradient, and crustal composition and thickness, *Geol. Soc. Spec. Publ.*, (28), 35–52.

Laslett, G. M., P. F. Green, I. R. Duddy, and A. J. W. Gleadow (1987), Thermal annealing of fission tracks in apatite 2 . A quantitative analysis, *Chem. Geol. (Isotope Geosci. Sect.*, *65*, 1–13, doi:10.1016/0168-9622(87)90057-1.

Levitte, D., J. Columba, and P. Mohr (1974), Reconnaissance Geology of the Amaro Horst, Southern Ethiopian Rift, *Geol. Soc. Am. Bull.*, *85*, 417–422.

Maccaferri, F., E. Rivaltas, D. Keir, and V. Acocella (2014), Off-rift volcanism in rift zones determined by crustal unloading, *Nature Geoscience*, *7*, 297–300.

Mbongo Djimbi, D., C. Gautheron, J. Roques, L. Tassan-Got, C. Gerin, and E. Simoni (2015), Impact of apatite chemical composition on (U-Th)/He thermochronometry: An atomistic point of view, *Geochim. Cosmochim. Acta*, *167*, doi:10.1016/j.gca.2015.06.017.

McConnell, R. B. (1972), Geological Development of the Rift System of Eastern Africa, *Geol. Soc. Am. Bull.*, *83*, 2549–2572.

McDowell, F.W., W. C. McIntosh, and K. A. Farley (2005), A precise 40Ar-39Ar reference age for the Durango apatite (U-Th)/He and fission track dating standard, *Chem. Geol. 214*, 249–263.

Mcleod, A. E., N. H. Dawers, and J. R. Underhill (2000), The propagation and linkage of normal faults: Insights from the Strathspey-Brent-Statfjord fault array, northern North Sea, *Basin Res.*, *12*(3–4), 263–284.

Meesters, A. G. C. A., and T. J. Dunai (2002), Solving the production – diffusion equation for finite diffusion domains of various shapes: Part II. Application to cases with α-ejection and nonhomogenous distribution of the source, *Chem. Geol.*, *186*, 347–363, doi:10.1016/S0009-2541(01)00423-5.

Mengesha, T., C. Tadiwos, and H. Workineh (1996), Explanation of the geological map of Ethiopia,

Mitchell, S. G., and P. W. Reiners (2003), Influence of wildfires on apatite and zircon (U-Th)/He ages, *Geology*, *31*(12), 1025–1028, doi:10.1130/G19758.1.

Mohr, P. A. (1962), *The geology of Ethiopia*, University College Addis Ababa Press, Addis Ababa.

Moore, J. M., and A. Davidson (1978), Rift Structure in Southern Ethiopia, *Tectonophysics*, *46*, 159–173.

Morewood, N. C., and G. P. Roberts (1999), Lateral propagation of the surface trace of the South Alkyonides normal fault segment, central Greece: its impact on models of fault growth and displacement-length relationships, *J. Struct. Geol.*, *21*, 635–652.

Morley, C. K. (1994), Interaction of deep and shallow processes in the evolution of the Kenya rift, *Tectonophysics*, *236*, 81–91.

Morley, C. K. (1999a), Basin Evolution Trends in East Africa, in *Geoscience of Rift Systems-Evolution of East Africa: AAPG Studies in Geology No. 44*, edited by C. K. Morley, pp. 131–150.

Morley, C. K. (1999b), Patterns of Displacement Along Large Normal Faults: Implications for Basin Evolution and Fault Propagation, Based on Examples from East Africa, *Am. Assoc. Pet. Geol. Bull.*, *83*(4), 613–634.

Morley, C. K. (1999c), Influence of Preexisting Fabrics on Rift Structure, in *Geoscience of Rift Systems-Evolution of East Africa: AAPG Studies in Geology No. 44*, edited by C. K. Morley, pp. 151–160.

Morley, C. K. (2002), Tectonic settings of continental extensional provinces and their impact on sedimentation and hydrocarbon prospectivity, *SEPM Spec. Publ.*, *73*, 22–56.

Morley, C. K. (2010), Stress re-orientation along zones of weak fabrics in rifts: An explanation for pure extension in 'oblique' rift segments?, *Earth Planet. Sci. Lett.*, *297*(3–4), 667–673, doi:10.1016/j.epsl.2010.07.022.

Morley, C. K., and W. A. Wescott (1999), Sedimentary Environments and Geometry of Sedimentary Bodies Determined from Subsurface Studies in East Africa, in *Geoscience of Rift Systems-Evolution of East Africa: AAPG Studies in Geology No. 44*, edited by C. K. Morley, pp. 211–231.

Morley, C. K., W. a. Wescott, D. M. Stone, R. M. Harper, S. T. Wigger, and F. M. Karanja (1992), Tectonic evolution of the northern Kenyan Rift, *J. Geol. Soc. London.*, *149*(3), 333–348, doi:10.1144/gsjgs.149.3.0333.

Morley, C. K., W. Bosworth, R. A. Day, R. Lauck, R. Bosher, D. M. Stone, S. T. Wigger, W. A. Wescott, D. Haun, and N. Bassett (1999a), Geology and Geophysics of the Anza Graben, in *Geoscience of Rift Systems-Evolution of East Africa: AAPG Studies in Geology No. 44*, edited by C. K. Morley, pp. 67–90.

Morley, C. K., D. M. Stone, R. M. Harper, and S. T. Wigger (1999b), Geology and Geophysics of the Western Turkana Basins , Kenya, in *Geoscience of Rift Systems—Evolution of East Africa: AAPG Studies in Geology No. 44*, edited by C. K. Morley, pp. 19–54.

Morley, C. K., D. K. Ngenoh, and J. K. Ego (1999c), Introduction to the East African Rift System, in *Geoscience of Rift Systems-Evolution of East Africa: AAPG Studies in*

Geology No. 44, edited by C. K. Morley, pp. 1–18.

Mortimer, E., L. A. Kirstein, F. M. Stuart, and M. R. Strecker (2016), Spatio-temporal trends in normal-fault segmentation recorded by low-temperature thermochronology: Livingstone fault scarp, Malawi Rift, East African Rift System, *Earth Planet. Sci. Lett.*, *455*, 62–72, doi:10.1016/j.epsl.2016.08.040.

Muirhead, J.D., S. A. Kattenhorn,H. Lee, S. Mana, B. D. Turrin, T. P. Fischer, and G. Kianji, (2016), Evolution of upper crustal faulting assisted by magmatic volatile release during early-stage continental rift development in the East African Rift, *Geosphere*, *12*, 1670-1700.

Noble, W. P., D. A. Foster, and A. J. W. Gleadow (1997), The post-Pan-African thermal and extensional history of crystalline basement rocks in eastern Tanzania, *Tectonophysics*, *275*(4), 331–350, doi:10.1016/S0040-1951(97)00026-7.

Nyblade, A. A. (1990), Terrestrial heat flow in east and southern Africa, *J. Geophys. Res. Solid Earth*, *95*(B11), 17371–17384.

Peacock, D., and D. J. Sanderson (1994), Geometry and Development of Relay Ramps in Normal Fault Systems, *Am. Assoc. Pet. Geol. Bull.*, *78*(2), 147–165, doi:10.1306/BDFF9046-1718-11D7-8645000102C1865D.

Philippon, M., G. Corti, F. Sani, M. Bonini, M. Balestrieri, P. Molin, E. Willingshofer, D. Sokoutis, and S. Cloetingh (2014), Evolution, distribution, and characteristics of rifting in southern Ethiopia, *Tectonics*, *33*, 1–24, doi:10.1002/2013TC003430.

Pik, R., B. Marty, J. Carignan, G. Yirgu, and T. Ayalew (2008), Timing of East African Rift development in southern Ethiopia □: Implication of topography, *Geology*, *36*(2), 167–170, doi:10.1130/G24233A.1.

Reiners, P. W., and M. T. Brandon (2006), Using Thermochronology to Understand Orogenic Erosion, *Annu. Rev. Earth Planet. Sci.*, *34*, 419–466, doi:10.1146/annurev.earth.34.031405.125202.

Reiners, P. W., and K. A. Farley (2001), Influence of crystal size on apatite (U-Th)/ He thermochronology: an example from the Bighorn Mountains, Wyoming, *Earth Planet. Sci. Lett.*, *188*, 413–420.

Reiners, P. W., T. A. Ehlers, and P. K. Zeitler (2005), Past, present, and future of thermochronology, *Revi*, *58*, 1–18, doi:10.2138/rmg.2005.58.1.

Reiners, P. W., S. N. Thomson, D. McPhillips, R. A. Donelick, and J. J. Roering (2007), Wildfire thermochronology and the fate and transport of apatite in hillslope and fluvial environments, *J. Geophys. Res. Earth Surf.*, *112*(4), doi:10.1029/2007JF000759.

Rousseeuw, P. J., and C. Croux (1993), Alternatives to the Median Absolute Deviation, *J. Am. Stat. Assoc.*, *88*(424), 1273–1283.

Rooney, T. O. (2017), The Cenozoic magmatism of East-Africa: Part I — Flood basalts and pulsed magmatism, *Lithos*, *286–287*, 264–301, doi:10.1016/j.lithos.2017.05.014.

Rowland, J. V., E. Baker, C. J. Ebinger, D. Keir, T. Kidane, J. Biggs, N. Hayward, and T. J. Wright (2007), Faullt growth at a nascent slow-spreading ridge: 2005 Dabbahu rifting episode, Afar, *Geophysical Journal International*, *171*(3), 1226–1246.

Royer, J.-Y., R. G. Gordon, and B. C. Horner-Johnson (2006), Motion of Nubia relative to Antarctica since 11 Ma: Implications for Nubia-Somalia, Pacific–North America, and India-Eurasia motion, *Geology*, *34*(6), 501–504, doi:10.1130/G22463.1.

Saria, E., E. Calais, D. S. Stamps, D. Delvaux, and C. J. H. Hartnady (2014), Present-day kinematics of the East African Rift, *J. Geophys. Res. Solid Earth*, *119*, 3584-3600, doi:10.1002/2013JB010901.

Schöpfer, M. P. J., C. Childs, and J. J. Walsh (2006), Localisation of normal faults in multilayer sequences, *J. Struct. Geol.*, *28*(5), 816–833.

Seiler, C., A. J. W. Gleadow, J. M. Fletcher, and B. P. Kohn (2009), Thermal evolution of a sheared continental margin: Insights from the Ballenas transform in Baja California, Mexico, *Earth Planet. Sci. Lett.*, *285*(1–2), 61–74, doi:10.1016/j.epsl.2009.05.043.

Shuster, D. L., R. M. Flowers, and K. A. Farley (2006), The influence of natural radiation damage on helium diffusion kinetics in apatite, *Earth Planet. Sci. Lett.*, *249*(3–4), 148–161, doi:10.1016/j.epsl.2006.07.028.

Smith, M., and P. Mosley (1993), Crustal Heterogeneity and Basement Influence on the Development of the Kenya Rift, East Africa, *Tectonics*, *12*(2), 591–606.

Soliva, R., and A. Benedicto (2004), A linkage criterion for segmented normal faults, *Journal of Structural Geology*, *26*, 2251–2267.

Steen, Ø., and A. Andresen (1999), Effects of lithology on geometry and scaling of small faults in Triassic sandstones, East Greenland, *J. Struct. Geol.*, *21*, 1351–1368.

Stern, R. J. (2002), Crustal evolution in the East African Orogen: a neodymium isotopic perspective, *J. African Earth Sci.*, *34*, 109–117.

Stern, R. J., K. C. Nielsen, E. Best, M. Sultan, R. E. Arvidson, and A. Kröner (1990), Orientation of late Precambrian sutures in the Arabian-Nubian Shield, *Geology*, *18*, 1103–1106, doi:10.1130/0091-7613(1990)018<1103.

Stockli, D. F. (2005), Application of Low-Temperature Thermochronometry to Extensional Tectonic Settings, *Rev. Mineral. Geochemistry*, *58*, 411–448, doi:10.2138/rmg.2005.58.16.

Stockli, D. F., K. A. Farley, and T. A. Dumitru (2000), Calibration of the apatite (U-Th)/He thermochronometer on an exhumed fault block, White Mountains, California, *Geology*, *28*(11), 983–986.

Storti, F., M. L. Balestrieri, F. Balsamo, and F. Rossetti (2008), Structural and thermochronological constraints to the evolution of the West Antarctic Rift System in central Victoria Land, *Tectonics*, *27*, 1–21, doi:10.1029/2006TC002066.

Stuart, G. W., I. D. Bastow, and C. J. Ebinger (2006), Crustal structure of the northern main Ethiopian rift from receiver function studies, *Geol. Soc. London Spec. Publ.*, *259*, 253–267, doi:10.1144/GSL.SP.2006.259.01.20.

Sullivan, P. B. O., and R. R. Parrish (1995), The importance of apatite composition and single-grain ages when interpreting fission track data from plutonic rocks: a case study from the Coast Ranges, British Columbia, *Earth Planet. Sci. Lett.*, *132*, 213–224.

Tagami, T., and C. Shinada (1996), Natural long-term annealing of the zircon fission track system around a granitic pluton, *J. Geophys. Res. Solid Earth*, *101*, 8,245-8,255.

Tentler, T. (2005), Propagation of brittle failure triggered by magma in Iceland, *Tectonophysics*, *406*(1-2), 17-38.

Torres Acosta, V., A. Bande, E. R. Sobel, M. Parra, T. F. Schildgen, F. Stuart, and M. R. Strecker (2015), Cenozoic extension in the Kenya Rift from low-temperature thermochronology: Links to diachronous spatiotemporal evolution of rifting in East

Africa, *Tectonics*, *34*(12), 2367–2386, doi:10.1002/2015TC003949.
Trudgill, B., and J. Cartwright (1994), Relay-Ramp forms and norma-fault linkages, Canyonlands National Park, Utah, *Geol. Soc. Am. Bull.*, *106*, 1143–1157.
Vauchez, A., G. Barruol, and A. Tommasi (1997), Why do continents break-up parallel to ancient orogenic belts?, *Terra Nov.*, *9*, 62–66.
Vauchez, A., A. Tommasi, and G. Barruol (1998), Rheological heterogeneity, mechanical anisotropy and deformation of the continental lithosphere, *Tectonophysics*, *296*, 61–86.
Vermeesch, P., and Y. Tian (2014), Thermal history modelling: HeFTy vs. QTQt, *Earth-Science Rev.*, *139*, 279–290, doi:10.1016/j.earscirev.2014.09.010.
Versfelt, J., and B. R. Rosendahl (1989), Relationships between pre-rift structure and rift architecture in Lakes Tanganyika and Malawi, East Africa, *Nature*, *337*, 354–357.
Vétel, W., and B. Le Gall (2006), Dynamics of prolonged continental extension in magmatic rifts: the Turkana Rift case study (North Kenya), *Geol. Soc. London Spec. Publ.*, *259*, 209–233.
Vétel, W., B. Le Gall, and J. J. Walsh (2005), Geometry and growth of an inner rift fault pattern: the Kino Sogo Fault Belt, Turkana Rift (North Kenya), *J. Struct. Geol.*, *27*, 2204–2222, doi:10.1016/j.jsg.2005.07.003.
Wagner, G., and P. Van den Haute (1992), *Fission-Track Dating*, Kluwer Academic Publishers, Dordrecht.
Walsh, J. J., A. Nicol, and C. Childs (2002), An alternative model for the growth of faults, *J. Struct. Geol.*, *24*, 1669–1675.
Walsh, J. J., W. R. Bailey, C. Childs, A. Nicol, and C. G. Bonson (2003), Formation of segmented normal faults: a 3-D perspective, *J. Struct. Geol.*, *25*, 1251–1262.
Wescott, W. A., S. T. Wigger, D. M. Stone, and C. K. Morley (1999), Geology and Geophysics of the Lotikipi Plain, *Geosci. Rift Syst. East Africa*, (44), 55–66.
Wildman, M., R. Brown, R. Beucher, C. Persano, F. Stuart, K. Gallagher, J. Schwanethal, and A. Carter (2016), The chronology and tectonic style of landscape evolution along the elevated Atlantic continental margin of South Africa resolved by joint apatite fission track and (U-Th-Sm)/He thermochronology, *Tectonics*, *35*(3), 511–545, doi:10.1002/2015TC004042.
Wilkins, S. J., and M. R. Gross (2002), Normal fault growth in layered rocks at Split Mountain, Utah: influence of mechanical stratigraphy on dip linkage, fault restriction and fault scaling, *J. Struct. Geol.*, *24*, 1413–1429.
Woldegabriel, G., and J. Aronson (1987), Chew Bahir Rift: A “failed” rift in southern Ethiopia, *Geology*, *15*, 430–433.
Woldegabriel, G., T. Yemar, G. Suw, T. Whrre, and B. Asfaw (1991), Age of volcanism and rifting in the Burji-Soyoma area, Amaro Horst, southern Main Ethiopian Rift: geo- and biochronologic data, *J. African Earth Sci.*, *13*(3/4), 437–447.
Woldegabriel, G., N. Hessen, and T. Yemane (1997), Agere Maryam Sheet (NB37-10), Geological Survey of Ethiopia, 1:250,000 scale.
Wolfe, M. R., and D. F. Stockli (2010), Zircon (U-Th)/He thermochronometry in the KTB drill hole, Germany, and its implications for bulk He diffusion kinetics in zircon, *Earth Planet. Sci. Lett.*, *295*(1–2), 69–82, doi:10.1016/j.epsl.2010.03.025.
Wolfenden, E., C. Ebinger, G. Yirgu, A. Deino, and D. Ayalew (2004), Evolution of the

northern Main Ethiopian rift: birth of a triple junction, *Earth Planet. Sci. Lett.*, *224*(1–2), 213–228, doi:10.1016/j.epsl.2004.04.022.

Yemane, T., and T. Yohunie (1987), *Geological Report on subsheets A, B, and C (Agere Mariam, NG-37-10)*, Addis Ababa.

Zanettin, B., E. Justin-Visentin, M. Nicoletti, and C. Petrucciani (1978), The evolution of the Chencha escarpment and teh Ganjuli graben (lake Abaya) in the southern Ethiopian rift, *Neues Jahrb. für Geol. und Palaontologie, 8*, 473–490.

Zeyen, H., F. Volker, V. Wehrle, K. Fuchs, S. V. Sobolev, and R. Altherr (1997), Styles of continental rifting: crust-mantle detachment and mantle plumes, *Tectonophysics*, *278*(1–4), 329–352, doi:10.1016/S0040-1951(97)00111-X.

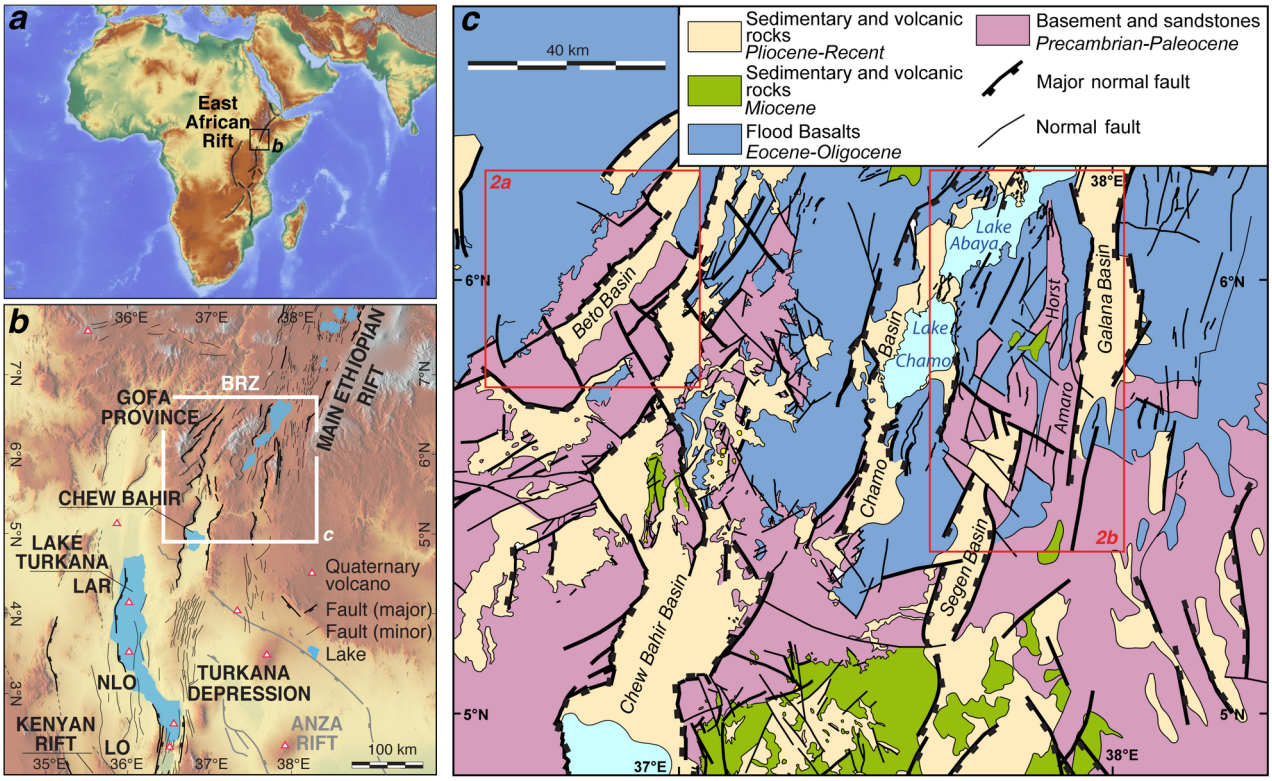

2018TC005210-f01-z-.tif

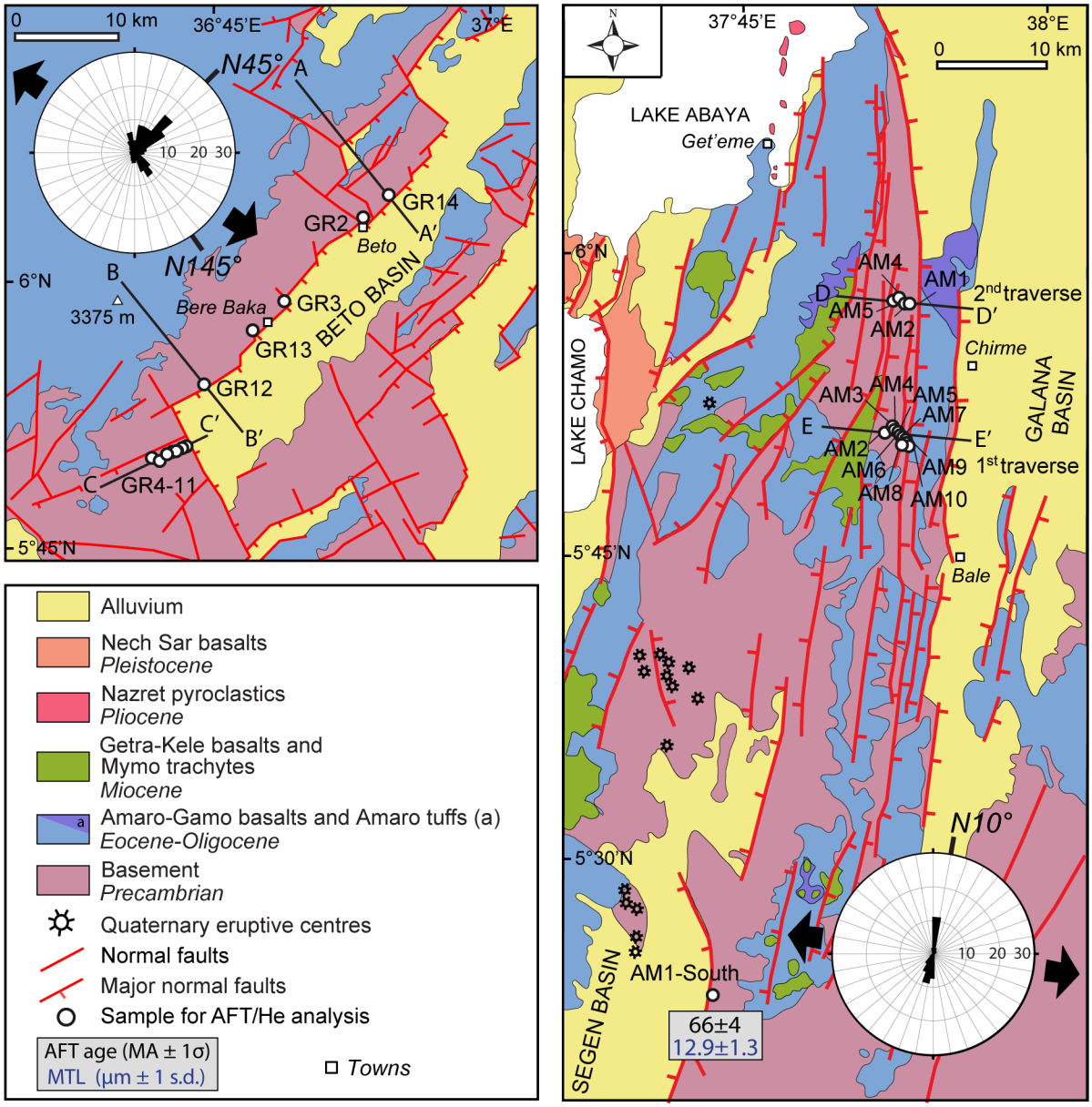

2018TC005210-f02-z-.tif

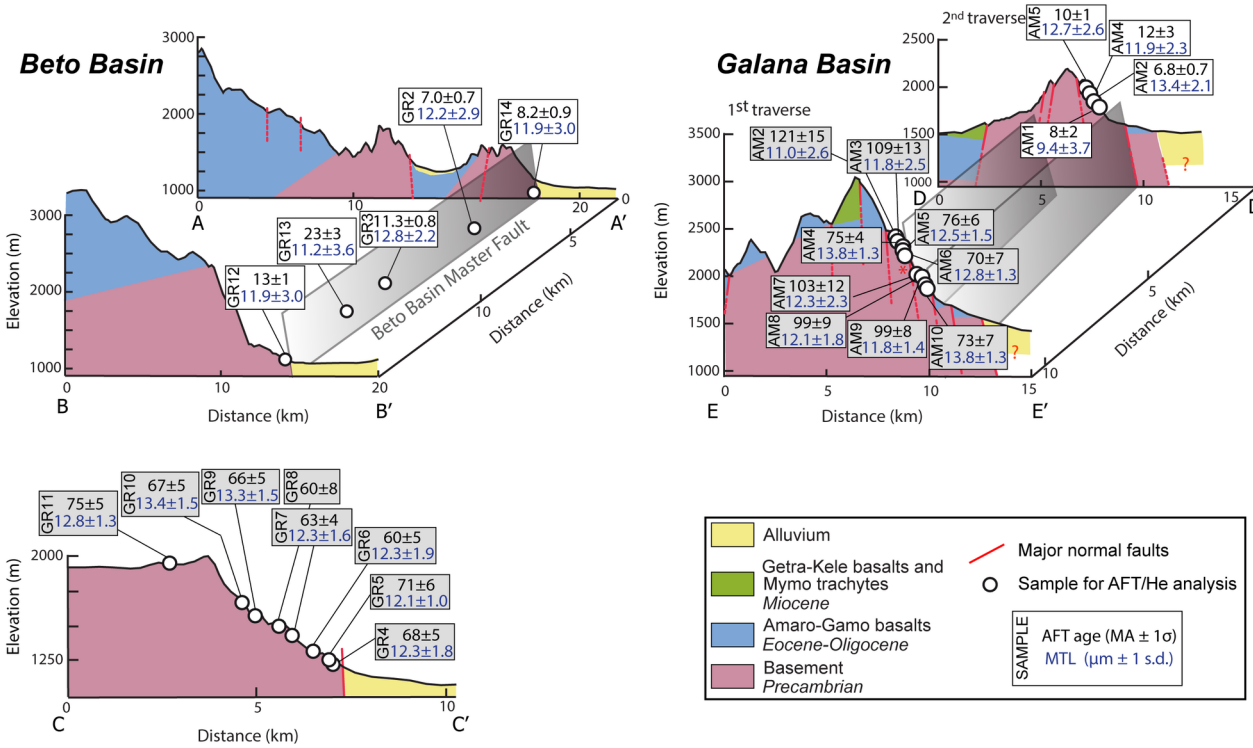

2018TC005210-f03-z-.tif

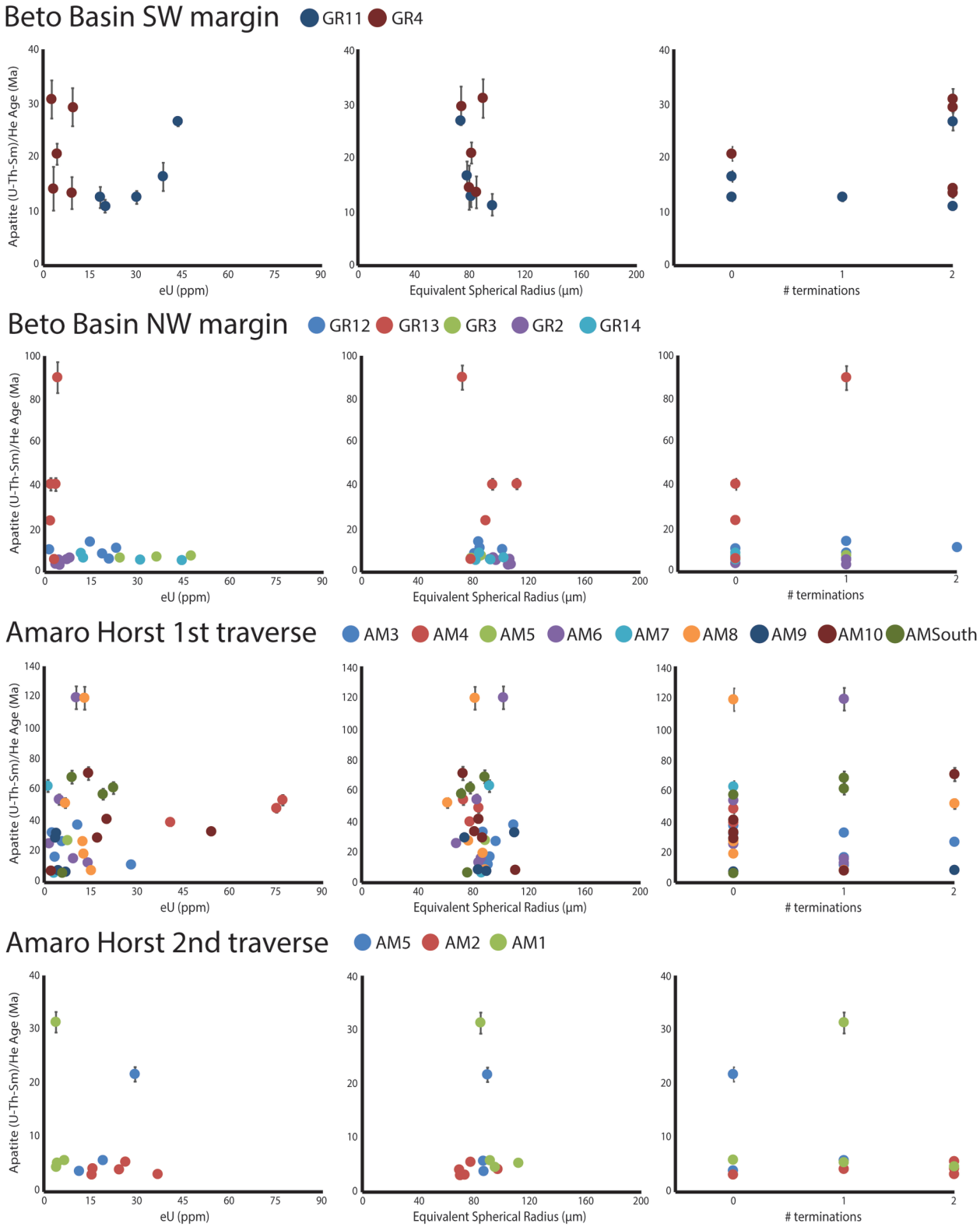

2018TC005210-f04-z-.tif

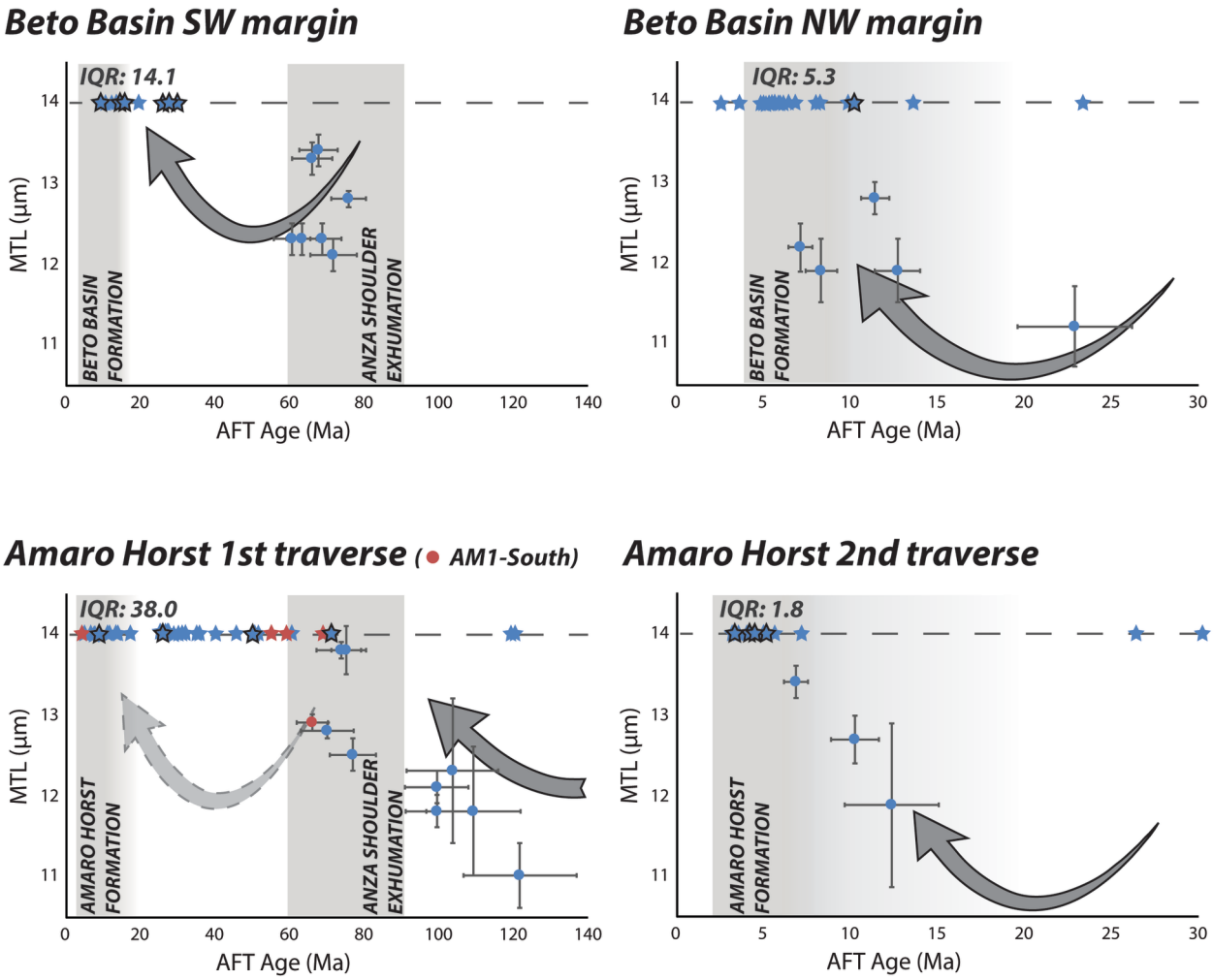

2018TC005210-f05-z-.tif

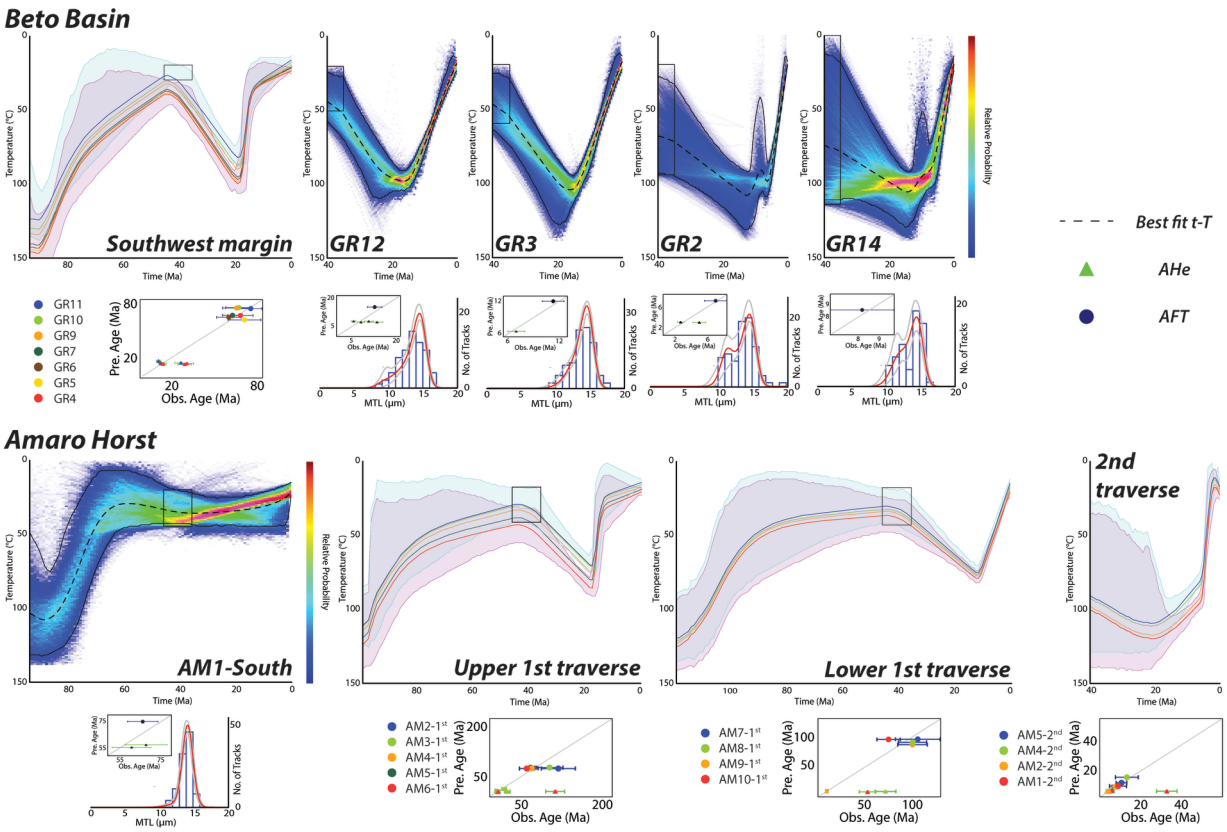

2018TC005210-f06-z-.tif

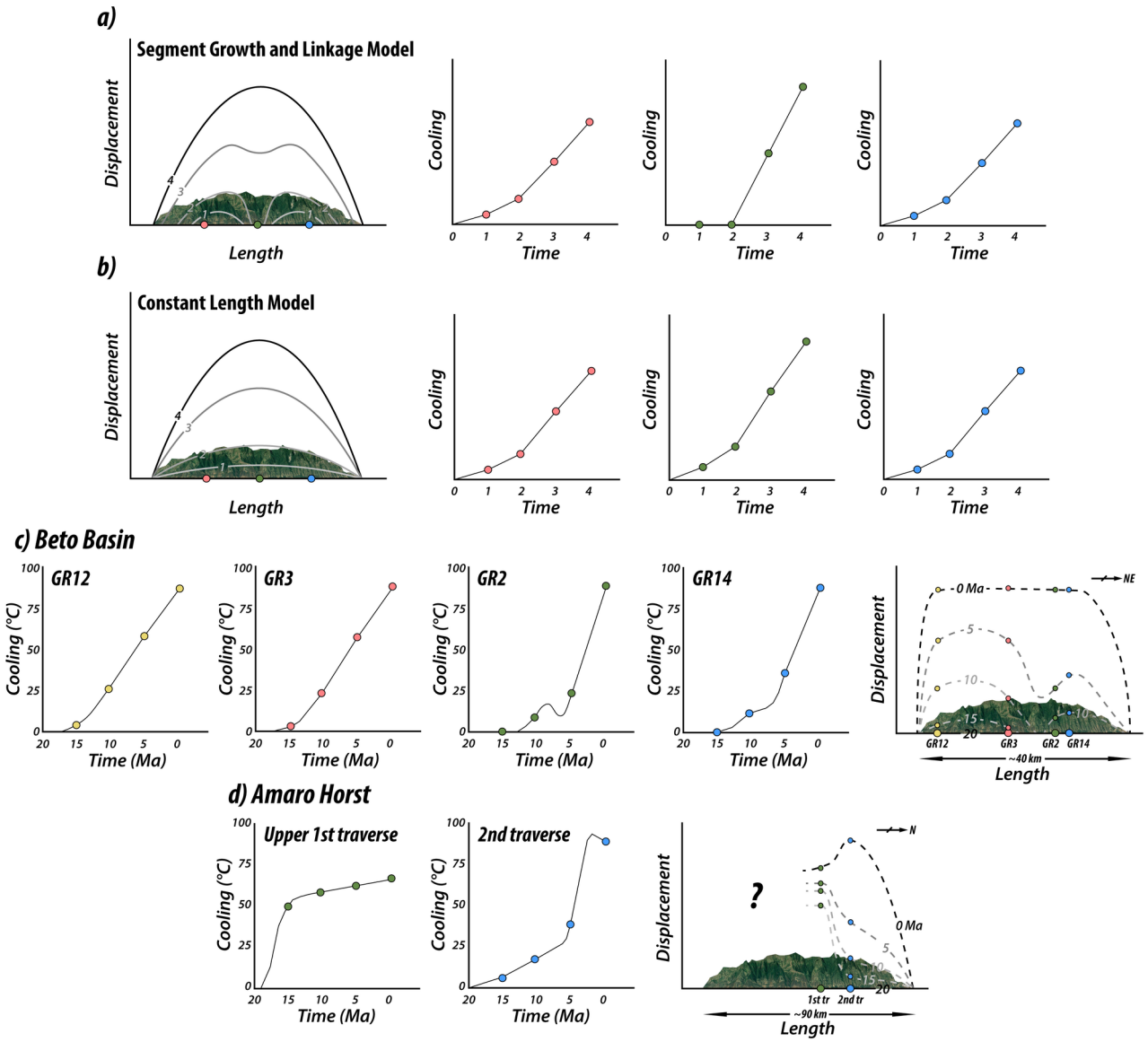

2018TC005210-f07-z-.tif